Acta Astronautica 202 (2023) 341–359

Contents lists available at ScienceDirect

Acta Astronautica

journal homepage: www.elsevier.com/locate/actaastro

Research paper

Using radar beam-parks to characterize the Kosmos-1408 fragmentation event

Daniel Kastinen [a,b,*], Juha Vierinen [c], Tom Grydeland [d], Johan Kero [a]

[a] Swedish Institute of Space Physics, Box 812, Kiruna, SE-98128, Sweden
[b] Department of Physics, Umeå University, Umeå University, Umeå, SE-90187, Sweden
[c] UiT the Arctic University of Norway, PO Box 6050 Langnes, Tromsø, N-9037, Norway
[d] NORCE Norwegian Research Centre, P.O.B 22 Nygårdstangen, Bergen, NO-5838, Norway

ARTICLE INFO

Keywords:
Space debris
Radar
SSA
SST
Kosmos-1408
ASAT

ABSTRACT

We describe the use of radar beam-park experiments to characterize the space debris resulting from a recent fragmentation event, the deliberate demolition of the defunct Kosmos-1408 satellite. We identify the Kosmos-1408 fragments and present distribution of measurement parameters as well as proxy orbit parameters. We present and apply a novel technique to estimate the size of objects by matching the signal to noise ratio of the detection to the radiation pattern of the radar. With this method we estimate the size distribution of the debris cloud. We also demonstrate how a pair of beam-park observations can be used to perform a crude, yet seemingly reliable, initial orbit determination. Finally, we present followup observations ~5 months after the fragmentation that show a still compact cloud of debris.

1. Introduction

Humanity's activities in space has had the unfortunate side-effect of leaving behind a sizable population of objects that no longer serve any purpose. These range in size from complete but defunct satellites (such as ENVISAT) and rocket stages, through fragments from explosions, collisions and other destructive events, small objects that have been lost or become detached, down to slag particles from solid–fuel rockets, and even flecks of paint. These objects are collectively known as space debris. Today, it is estimated that there are on the order of 1 million objects larger than 1 cm in orbit [1–3], and the European Space Agency (ESA) estimates that the total mass currently in Earth orbit is on the order of 10,000 tonnes [3,4].

When collisions occur between objects at the typical orbital velocities in Earth orbit, e.g. ~8 km/s for Low Earth Orbit (LEO), even a small screw can severely damage a satellite or disturb a scientific measurement. Fragmentation events, such as collisions between fragments, occur all the time, and result in the breakup of large objects into multitudes of smaller objects.

The space debris population poses a critical risk for active satellites and space missions. Collisions with debris may damage valuable infrastructure in space and cause a catastrophic chain reaction of fragmentation events. Unless the problem can be brought under control, the density of debris will at some point be high enough that collisions are unavoidable in some of these orbital regimes. The cascading chain reaction of collisions will then reduce all objects in those regimes to debris on a time scale "much shorter than years".[1] The debris environment left after such a cascade can potentially make human space activities (unmanned as well as manned) infeasible for centuries. [5–8].

Space debris also poses a risk to infrastructure and life on the Earth's surface. A de-orbiting debris object could survive re-entry through the atmosphere and strike the surface of the Earth [9]. Several large pieces of space debris have already been recovered on the ground, but none of these events have this far caused any human casualties [10]. Additionally, during re-entry the ablated material constitutes an ever growing anthropogenic injection of compounds into the atmosphere which could have unforeseen consequences [11,12].

For all of these reasons it is desirable to track, understand and model the debris population and fragmentation events. This is so that active satellites and other infrastructure in space can be maintained, collisions avoided and an exponential growth of space debris averted [13].

Space debris is a fairly new phenomenon, one that started when contact was lost with Sputnik 1 on 26 October 1957. Even so, a

* Corresponding author.
E-mail addresses: daniel.kastinen@irf.se (D. Kastinen), juha-pekka.vierinen@uit.no (J. Vierinen), tgry@norceresearch.no (T. Grydeland), kero@irf.se (J. Kero).

[1] Kessler, Donald J. (8 March 2009). "The Kessler Syndrome". https://web.archive.org/web/20100527195029/http://webpages.charter.net/dkessler/files/KesSym.html

https://doi.org/10.1016/j.actaastro.2022.10.021
Received 2 June 2022; Received in revised form 29 September 2022; Accepted 9 October 2022
Available online 22 October 2022

significant collection of radar observations are beginning to accumulate from a multitude of systems [14]. Such observations have already been used to create multiple iterations of debris and fragmentation models [2,15,16].

These radar systems penetrate beyond the ionosphere of the Earth, which allows the transmitted radio waves to scatter off resident space objects (RSOs), thereby generating echoes. These echoes can then be coherently integrated to determine several parameters, most commonly range, range-rate and radar cross section (RCS) [17]. For measuring the RSO population monostatic radar measurements with a stationary antenna beam pointing direction (hereafter beam-park observations) are the most common observing mode [14,18,19]. Beam-parks of the debris environment have previously been used to detect and partially characterize fragmentation events [18,20].

In this study we have conducted beam-park observations using the EISCAT UHF and Svalbard radar to characterize the debris cloud generated by the deliberate destruction of the Kosmos-1408 satellite on the 15th of November, 2021. Kosmos-1408 was destroyed in a so called direct-ascent anti-satellite test by Russia. The Russian Defense Ministry has not officially revealed which system was used to facilitate the destruction. The set of observational campaigns were conducted during a ten-day period November 19th through 29th, 2021, and an additional campaign was performed as a follow-up study on April 5th, 2022. It is desirable to explore the limits of what and how much information can be derived from such measurements. Here, we explore those limits by analyzing the beam-park observations focusing on orbit information and size estimates for individual objects, as well as statistical orbit information and size distributions. We have not explored fragmentation parameter estimation nor debris number density estimation as this requires an additional layer of modeling outside the current scope. However, such considerations are a direct next step that could be taken using the results presented here.

Fragments from the Kosmos-1408 destruction will remain a threat to infrastructure in space for years to come and raise the need for collision avoidance manoeuvres, such as that performed with Sentinel-1 A on May 16th, 2022.[2]

2. EISCAT beam-park experiment

2.1. EISCAT UHF

The EISCAT UHF system was originally built in 1978 as a tristatic radar for ionospheric observations, with a transmitter/receiver site outside Tromsø, Norway (69°35′N, 19°14′E) and receive-only sites near Kiruna, Sweden (67°52′N, 20°26′E), and Sodankylä, Finland (67°22′N, 26°38′E). The radar was built to operate at a center frequency of 933 MHz, with about 1 MHz of maximum usable transmit bandwidth. Each site comprises a fully steerable Cassegrain-type dish antenna with a 32 m diameter main reflector and a nominal gain of 48.1 dB. Due to interference, the operating frequency of the system has been shifted several times during its operational lifetime. During the 2021 measurements reported here the frequency was set to 929 MHz. During the 2022 campaign it was set to 927.5 MHz. Interference also caused the remote stations to be refurbished for use with a different EISCAT system. Hence, they could not be used for our measurements.

The UHF radar can deliver 2 MW of transmit power, and at the frequency of 930 MHz, this means that a calibration target at a range of 1000 km will have to have a diameter of 1 cm to scatter power equal to the system noise. We refer to this measure as *noise-equivalent diameter* [18], and it is a convenient performance metric for comparing radar systems. In Fig. 1 the noise-equivalent diameter is illustrated as function of range for the radar systems that were used for space debris observations in the current study.

[2] https://twitter.com/esaoperations/status/1526919484753182722

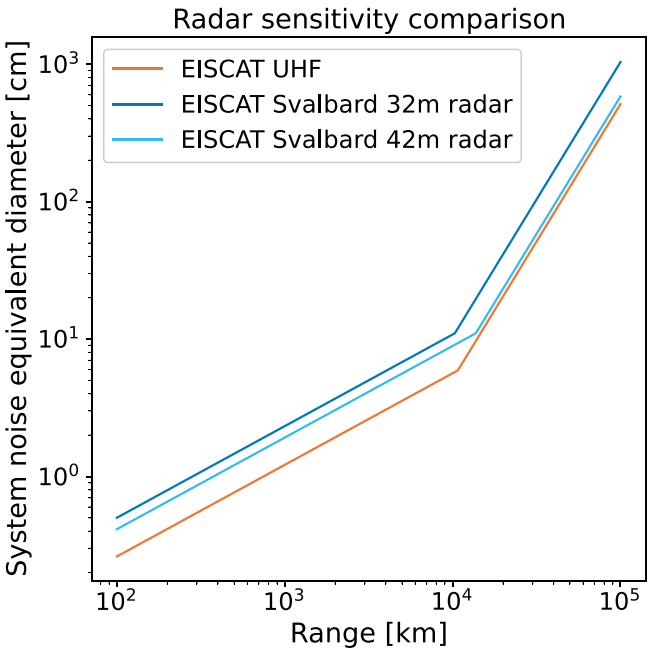

Fig. 1. Noise-equivalent diameter (see text for details) as function of slant range for the radar systems in the current study.

2.2. EISCAT Svalbard Radar

The EISCAT Svalbard Radar (ESR), inaugurated in 1996, extended EISCAT observations into the polar regions. It is located at 78°9′N, 16°1′E, outside Longyearbyen on the island of Spitsbergen in the Svalbard archipelago. It comprises a fully steerable Cassegrain-type antenna with a 32 m diameter main reflector, and a 42 m diameter antenna (added in 1999) fixed to point in the direction of the Earth's magnetic field. It features a 1 MW transmitter (upgraded from 500 kW in 1998) at a center frequency of 500 MHz. The longer wavelength means that even though the antenna has as much collecting area as the UHF radar, the gain is lower. The gain is 42.5 dB for the steerable antenna and 44.8 dB for the fixed antenna. The noise-equivalent diameters are 2.3 cm and 1.9 cm at 1000 km, respectively (cf. Fig. 1).

2.3. Experiment description

The experiment used for observing space debris at EISCAT is code-named LEO. The LEO experiment uses a 64-bit code with 30 μs bauds, which nominally means a range resolution of around 4.5 km. The inter pulse period is 20 ms, which provides coverage to beyond 2500 km of slant range. A complete cycle of the code is completed after 128 pulses or 2.56 s, and data from the mode in correlated and integrated format is dumped after 5 cycles, or every 12.8 s. For the purpose of hard target detection, data are also saved in raw format (pre-integrated amplitude-level data) and processed off-line.

At EISCAT UHF, the radar was pointed towards 75° elevation and 90° azimuth (due East). This pointing direction gives good discrimination between ascending and descending orbits, without undue extension of range for a given target altitude. Furthermore, this pointing direction has been used for more than a decade of beam-park observations with the UHF, so for the purpose of building comparable observations over time, it should not be changed without a compelling reason.

At the ESR, two different pointing directions were used with the 32 m antenna. These are listed in Table 1. The 42 m antenna is fixed to the direction of local magnetic zenith, azimuth 185.5° and elevation 82.1°.

Table 1
Summary of pointing directions, duration, and number of events extracted in the analysis of the beam-park experiments performed at three different radar systems. The total number of events is also split into the categories *K1408* for Kosmos-1408 fragments and *Other* for the background population, for all correlated and uncorrelated events, as further described in Section 4.1.

Radar	Azimuth	Elevation	Start time [UT]	Hours	Total	Events			
						Correlated		Uncorrelated	
						K1408	Other	K1408	Other
UHF	90.0	75.0	2021-11-23 10:00	7.0	756	2	277	113	364
			2021-11-25 10:04	6.9	598	5	304	80	209
			2021-11-29 08:00	24.0	1710	3	969	165	573
			2022-04-05 13:44	24.0	1481	–	–	–	–
ESR(32)	90.0	75.0	2021-11-19 19:00	24.0	2718	19	2087	269	343
			2021-11-23 10:00	7.0	772	8	600	71	93
ESR(42)	185.5	82.1	2021-11-25 10:04	3.8	396	9	263	39	85
			2021-11-29 08:19	7.4	923	21	673	123	106
			2022-04-05 12:00	23.9	1900	–	–	–	–

3. Methodology

3.1. Signal analysis

The data collected during the radar experiments were analyzed using the methods described in detail by Markkanen et al. [17].

3.2. Gain model

The EISCAT UHF antenna radiation pattern was measured making use of a boresight tower as part of the acceptance test after delivery. We have used the right hand side of the measured pattern given in Diagram 17 of the acceptance test report [21] and assumed circular (azimuthal) symmetry to define the gain model, which is displayed in Fig. 16 of the current paper. In reality, the gain pattern of the antenna is not circularly (azimuthaly) symmetric due to the three support legs of its 4.58 m subreflector, which shade the main 32 m reflector.

We have not found a similar measured antenna pattern for the ESR, and hence we use a standard Cassegrain model.[3] For more information see Balanis [22], section 15.4, and references therein.

3.3. Correlation

Performing correlation analysis between beam-park measurements and a catalogue of known objects is very beneficial for further analysis and validation purposes. Correlation analysis attempts to attribute measurements to objects from a given catalogue. Hence, uncorrelated measurements are possibly from previously unknown objects. This information allows for removal of the background population that is not in the focus of the current study as well as providing a reference set of previously known objects that can be used as validation objects for e.g. the RCS estimation method described below.

To perform the correlation analysis we have used the Two-Line Element (TLE) archives of space-track.[4] We fetch the entire TLE catalogue for the 24 h prior to the start of the beam-park. When there are multiple TLEs for the same object, we choose the one closest to the observation window. We then propagate each object, indexed by j, in the catalogue using the SGP4 propagator for the duration of the campaign and simulate measurement data, range r_{ij} and range-rate v_{ij}, for the time of each measurement t_i. The summary data from the beam-park-experiment analysis produces only one range and range-rate for the peak signal to noise ratio (SNR) of the measurement set, $\tilde{r}_i$ and $\tilde{v}_i$. Hence we treat each measurement time t_i as belonging to a possibly separate RSO. We then calculate a weighted total residual as

$$d_{ji} = \sqrt{\left(\frac{r_{ij} - \tilde{r}_i}{W_r}\right)^2 + \left(\frac{v_{ij} - \tilde{v}_i}{W_v}\right)^2}. \quad (1)$$

The weights W_r and W_v were chosen to be $W_r = 1$ and $W_v = 0.2$. These weights were empirically determined based on previous correlation attempts and the typical range versus velocity differences in LEO-orbits [e.g.23]. The correlation process is identical if we instead had used time-series for each detected object. The only difference would be to calculate the mean of the residuals over time instead. For example, the range component $(r_{ij} - \tilde{r}_i)^2$ would be replaced by $N^{-1}\sum_{l=1}^{N}(r_{ijl} - \tilde{r}_{il})^2$ where N is the size of the time-series. For each measurement, the smallest distance and the object that produced that distance is chosen, $d_i = \min_j d_{ij}$ and $j_i = \mathrm{argmin}_j d_{ij}$.

The set of distances d_i consists of two distinct populations. The first population consists of measurements from objects not in the catalogue, resulting in the closest unrelated object being chosen as the best one. This population generates a distribution with large distances. The second population generates a distribution with small distances where the object that produced the measurement did exist in the catalogue. Even catalogued objects result in a non-zero distance due to inaccurate or outdated catalogue entries, errors in the propagation, errors in the measurements and from possible manoeuvres by active objects.

These two populations together create a bi-modal distribution that can be approximated by log-normal distributions. To determine a threshold D_{max} that separates these two populations, thereby selecting which measurements were correlated and which were not, we fitted a bi-modal normal distribution to the histogram function of $\log_{10}(d_i)$. The intersection point of the two normal distributions given the fit minimizes the false positive and false negative rates. Hence, any measurement with correlation distance $d_i < D_{max}$ was determined as likely belonging to the known object j_i. We analyze each measurement campaign individually in this manner as we want to avoid any shift in the two normal distributions due to e.g. a change in geometry or in system parameters.

As an example, the $\log_{10}(d_i)$ distribution for the correlation analysis of the UHF campaign on 2021-11-23 is illustrated in Fig. 2 together with the estimated threshold.

To further improve the correlation process we included an additional feature in the propagation stage of the correlation. The most common error in the TLE-catalogue is a small offset in mean anomaly, mainly caused by poor estimation of the area-to-mass ratio and/or modeling of the atmospheric density. To compensate we introduced a small time-offset during propagation so that each TLE was displaced in start time by a maximum of ±5 seconds with 11 steps. Then the best match in d from these 11 different propagation points were chosen as the d_{ij} value for that object.

[3] https://github.com/danielk333/pyant
[4] https://space-track.org

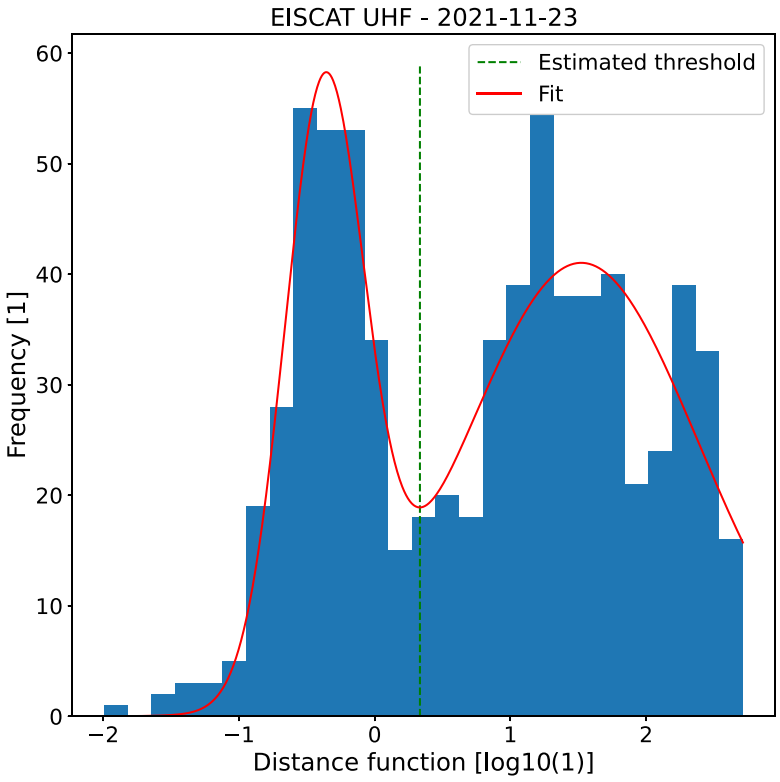

Fig. 2. Distribution of the log minimum distances $\log_{10}(d_i)$ for each detection during the EISCAT UHF measurement campaign conducted on 2021-11-23, as well as the estimated threshold for selecting successful correlations.

3.4. Radar cross section estimation

The RCS of targets usually cannot be determined without accurate knowledge of the position of the target and the antenna radiation pattern. Positional information cannot be directly determined during monostatic beam-park observations, instead one usually calculates a lower limit on RCS. This is done by assuming that the peak SNR detection of the object is made at the maximum of the antenna gain pattern. As such, any other position would imply a larger target RCS. This assumption also solves the problem of accurate radiation pattern models as the main lobe is usually very well modeled and characterized while side-lobes are often not [21].

The RCS of an object can be estimated using the radar equation [17],

$$\mathrm{RCS} = \frac{E_{\mathrm{rx}}(4\pi)^3 k T_{\mathrm{sys}} R^4}{P_{\mathrm{tx}} G_{\mathrm{tx}}(\hat{\mathbf{k}}) G_{\mathrm{rx}}(\hat{\mathbf{k}}) \lambda^2 T_{\mathrm{coh}}}, \tag{2}$$

where E_{rx} is the measured signal energy, P_{tx} is the transmitted power, $G_{\mathrm{rx}}(\hat{\mathbf{k}})$ and $G_{\mathrm{tx}}(\hat{\mathbf{k}})$ are the receiver and transmitter gain patterns, λ is the wavelength, k the Boltzmann constant, T_{sys} the receiver noise temperature, R the range to the target and T_{coh} the total signal length that is coherently integrated, i.e. including the duty-cycle of the experimental setup.

With the measured signal energy, Eq. (2) can be used together with a scattering model to estimate the size of the target. We have used the scattering model described in Markkanen et al. [24] and Morchin [25]. This model approximates the target as a sphere and transitions directly from the optical regime to the Rayleigh regime, ignoring the oscillating Mie regime. We motivate this approximation with the (realistic) assumption that the majority of the error in any size estimation stems from the object shape, material, position in the radar beam and the beam characterization itself. Our approach is similar to the one employed by NASA in their Size Estimation Model. The NASA model data, as presented in Hamilton et al. [Figure 1 26], is based on a set of representative debris pieces measured in an anechoic chamber. Their data show RCS variation on the order of the Mie oscillations of a perfectly reflecting sphere; but, spread around the optical approximation. Hence, as we generally have no a priori knowledge of the shapes or compositions of the objects being measured, the smallest error in a statistical sense is achieved by ignoring Mie scattering. The diameter d can then be expressed as

$$d = \begin{cases} \left(\frac{4\lambda^4}{9\pi^5}\mathrm{RCS}\right)^{\frac{1}{6}} & \forall\ d < \frac{\lambda}{\pi\sqrt{3}} \\ \left(\frac{4}{\pi}\mathrm{RCS}\right)^{\frac{1}{2}} & \forall\ d \geq \frac{\lambda}{\pi\sqrt{3}} \end{cases} \tag{3}$$

As opposed to other transient targets, such as meteors [27], the RCS of an RSO can be approximated as constant during the measurement if we ignore the possible rotation states of asymmetrically shaped objects [28,29]. The range is determined at each point of measurement and hence the variation of this parameter can be accounted for. Rearranging Eq. (2) to represent received power

$$P_{\mathrm{rx}} = \frac{E_{\mathrm{rx}}}{T_{\mathrm{coh}}} = \mathrm{RCS}\frac{P_{\mathrm{tx}} G_{\mathrm{tx}}(\hat{\mathbf{k}}) G_{\mathrm{rx}}(\hat{\mathbf{k}}) \lambda^2}{(4\pi)^3 k T_{\mathrm{sys}} R^4}, \tag{4}$$

we can see that the largest influence on received power P_{rx}, and hence SNR, is the path through the gain pattern as a function of time $\hat{\mathbf{k}}(t)$. This indicates that the measured SNR curve $\tilde{S}(t)$ contains information about $\hat{\mathbf{k}}(t)$. If the assumptions hold that the accuracy of the gain model G is sufficient and that the gain pattern contains enough unique features between different paths $\hat{\mathbf{k}}(t)$, one can infer $\hat{\mathbf{k}}(t)$ from $\tilde{S}(t)$. This principle applied on beam-park measurements can provide a direct diameter estimation, rather than a lower limit, and a limited range of possible diameters based on the path taken by the object through the gain pattern.

To explore if such an approach is possible we developed a technique using a normalized weighted L^2-norm on the difference between the normalized measured SNR curve and a set of simulated normalized SNR curves $S(\hat{\mathbf{k}}(t))$. The normalizations of the SNR curves are with respect

to the peak SNRs $\tilde{S}_{\text{peak}} = \max_j \tilde{S}_j$ and $S_{\text{peak}} = \max_j S_j$, i.e. $\hat{\tilde{S}}_j = \tilde{S}_j \tilde{S}_{\text{peak}}^{-1}$ and $\hat{S}_j = S_j S_{\text{peak}}^{-1}$. This L^2-norm D functions as a distance measure between the simulated path and the measured path and can be expressed as

$$D^2 = \frac{1}{N}\left(d_{\text{cut}} + d_{\text{miss}} + d_{\text{hit}}\right), \tag{5}$$

where the main body of detections are included in d_{hit} as

$$d_{\text{hit}} = \sum_{j\in J} \hat{w}_j^2 \left(10\log_{10}(\hat{\tilde{S}}_j) - 10\log_{10}(\hat{S}_j)\right)^2. \tag{6}$$

Here N is the total number of measurement points. The set of used detections J are those that are above the SNR limit in both measurement and simulation. Using the SNR limit, we create a normalized limit relative to the peak SNR to apply this relative limit to the simulated normalized curves. The distance function in Eq. (5) is normalized by N to make comparison between events of different length possible. The difference is taken in units of dB as this better represents the shape of the SNR curves that span over several orders of magnitude.

The point-weighting $\hat{w}_j$ is included to compensate for the uncertainty in the model gain pattern of the radar. As was previously discussed, the main and first side-lobes are usually well characterized but far off-axis side-lobes are not. Hence this weighting will encode that uncertainty and is defined as

$$\hat{w}_j = \frac{w_j}{C},\ w_j = \frac{1}{\theta_j + 1 - \theta_{\min}}, \tag{7}$$

$$\theta_{\min} = \min_{j\in[1,N]} \theta_j,\ C = \sum_{j=1}^{N} w_j, \tag{8}$$

$$\theta_j = \angle(\hat{\mathbf{k}}_{\text{bore-sight}}, \hat{\mathbf{k}}(t_j)), \tag{9}$$

where θ is the angle from bore-sight, i.e. the off-axis angle. In practical terms, this weight makes differences between the measured and the simulated SNR pattern more important the closer we are to the main lobe.

The additional distances d_{cut} and d_{miss} are designed to take the effect of a "noise floor" into account, based on the SNR limit. d_{cut} represents a distance penalty for simulated detections above the SNR limit where there are none in the measured signal,

$$d_{\text{cut}} = \sum_{j\in J_{\text{cut}}}^{N} \hat{w}_j^2 \left(10\log_{10}(\hat{S}_j) - 10\log_{10}(\hat{S}_{\text{lim}})\right)^2. \tag{10}$$

Here the selection of detections J_{cut} is done by examining which simulated detections are above the SNR limit S_{lim} while at the same time are below in the measured detections. d_{miss} represents a distance penalty for simulated detections below the SNR limit where there are detections above the limit in the measured signal,

$$d_{\text{miss}} = \sum_{j\in J_{\text{miss}}}^{N} \left(\hat{w}_j 10\log_{10}(\hat{\tilde{S}}_j)\right)^2. \tag{11}$$

Here the selection J_{miss} are simulated detections that are below the SNR limit while at the same time are above in the measured detections.

What remains is to parametrize the different simulated SNR curves $S(\hat{\mathbf{k}}(t))$. To reduce the dimensionality of the problem we assume the path follows a circular orbit. Further, we assume the gain pattern is circularly symmetric. As such, we can generate a representative set of orbits by propagating circular orbits parameterized on perturbations in inclination δi and true anomaly $\delta\nu$. The original circular orbit is constructed by assuming the target is at the center of the pointing direction and using the measured range at peak SNR. This provides us with the base case of the object in bore-sight, its position is $\mathbf{r}_{\text{bore-sight}} = \mathbf{r}_{\text{ECEF-radar}} + R_{\text{max-SNR}}\hat{\mathbf{k}}_{\text{ECEF-bore-sight}}$. The orbit is assumed to be circular and we pick any velocity vector $\mathbf{v}_{\text{bore-sight}}$ perpendicular to $\mathbf{r}_{\text{bore-sight}}$ with magnitude $v = \sqrt{\frac{\mu_{\text{Earth}}}{a}}$. The inclination and true anomaly perturbations will then generate a set of trajectories representative of all possible measured SNR curves. From each of these proxy orbits we can determine an estimated size and its distance value, i.e. how close to the actual measurement it was.

In Fig. 3 an example comparison between a measured and a simulated SNR curve is illustrated. In the title the different sub-distances are printed together with the total distance D. This was the best match for this event. The sub-distances are NaN if the set J is empty and are then ignored. The estimated diameter for each point in the time-series, given the position in the beam pattern, is also illustrated in Fig. 3. For this matching trajectory the size estimate is stable around ≈ 25–35 cm while in the main lobe. The divergence around the theoretical gain minimum is due to deviation of the true radiation pattern from the modeled one. This example can only be put into context when it is compared with all other proxy trajectories. The map $D(\delta i, \delta\nu)$ between proxy orbit $\delta i, \delta\nu$ and distance D is illustrated in Fig. 4. We can here see that there is a small spread of proxy orbits that match well with the measurements. Selecting only this region of close matches we can use the trajectory from each proxy orbit to estimate the diameter of the object. This selection and estimation is illustrated in Fig. 5, which shows that the possible matches with low distances result in sizes between ≈ 20–40 cm. It should be noted that there are larger uncertainties present in this size estimation than just the variation of the matching function. As mentioned before, object rotation and the radar gain pattern models are large sources of uncertainty, although these sources combined should not exceed an order of magnitude in size uncertainty if the object passed the main lobe of the beam. This particular event was correlated to a known catalogue object, thus allowing a prediction of the trajectory and the estimation of the diameter at peak SNR. This prediction is illustrated in Fig. 6. We can see here that the predicted diameter is ≈120–150 cm but the match between the side-lobe detections of the simulated SNR and the measured SNR is significantly worse for the TLE predicted than with the SNR curve matching illustrated in Fig. 3. This mismatch could be caused by a relatively small error in the original TLE, or by errors in the gain model. However, it is not possible to determine which of the diameter estimated from TLE predictions or diameter estimated from SNR curve matching is correct without e.g. high precision GPS data of the target or a prior size estimate. Either way, a size estimate within a factor of 2 using only monostatic single channel data is a significant improvement from a lower limit on diameter only.

Of course this parameterization relies on the fact that the gain pattern is circularly symmetric and that the orbits are not very eccentric. These orbits are not supposed to be representative of the actual orbit of the object, instead they act as a convenient parameterization of the input space.

A more generalized trajectory model can be constructed by picking any two points at the start t_0 and end t_1 of the measurement series, i.e. $R(t_0)\hat{\mathbf{k}}_0$ and $R(t_1)\hat{\mathbf{k}}_1$. The Lambert problem can then be solved using these two points in space and the time of flight $\Delta t = t_1 - t_0$ [30].[5] The solution yields the orbit that intersects with the two chosen points. Then this orbit would be used to generate the path $\hat{\mathbf{k}}(t)$. However, in this case the input parameter space to the set of trajectories would be 4-dimensional, two for $\hat{\mathbf{k}}_0$ and two for $\hat{\mathbf{k}}_1$, instead of the 2-dimensional one we have used here.

3.5. Inclination and semi-major axis identification

Direct initial orbit determination (IOD) is not possible from a single beam-park measurement only. Therefore, different assumptions have previously been used to derive orbital characteristics. Most common is the assumption of circular orbits. E.g., Stansbery et al. [31] used this method to identify inclination and semi-major axis populations of the debris environment.

[5] https://github.com/jorgepiloto/lamberthub

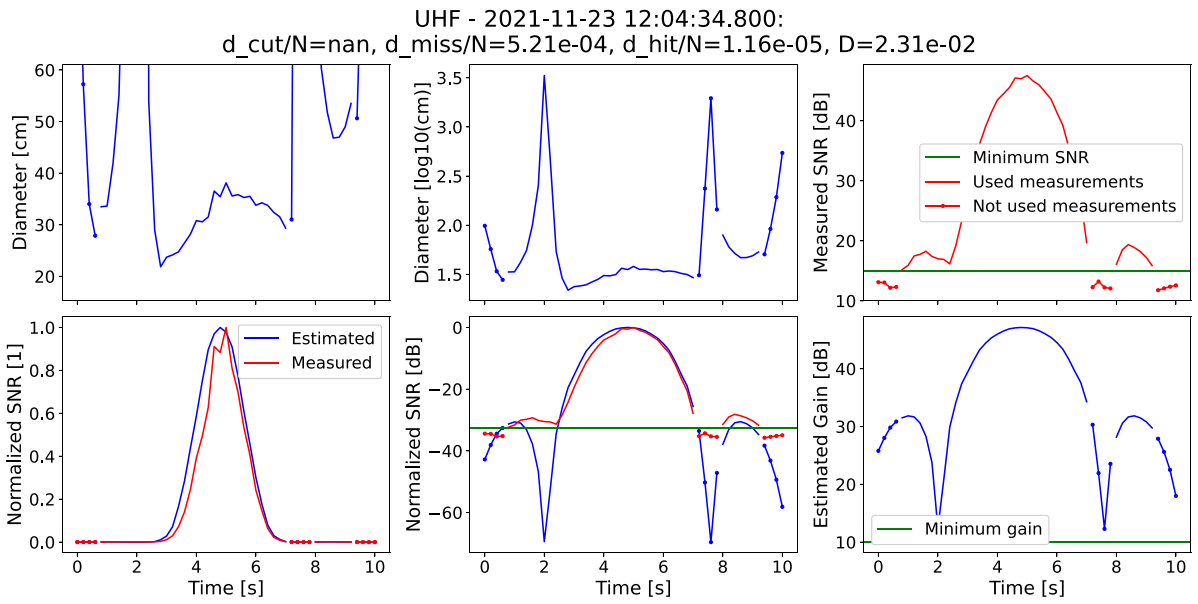

Fig. 3. Comparison between simulated SNR curve and a measured SNR curve using the circular proxy orbit trajectory as well as the distance function value for this particular trajectory.

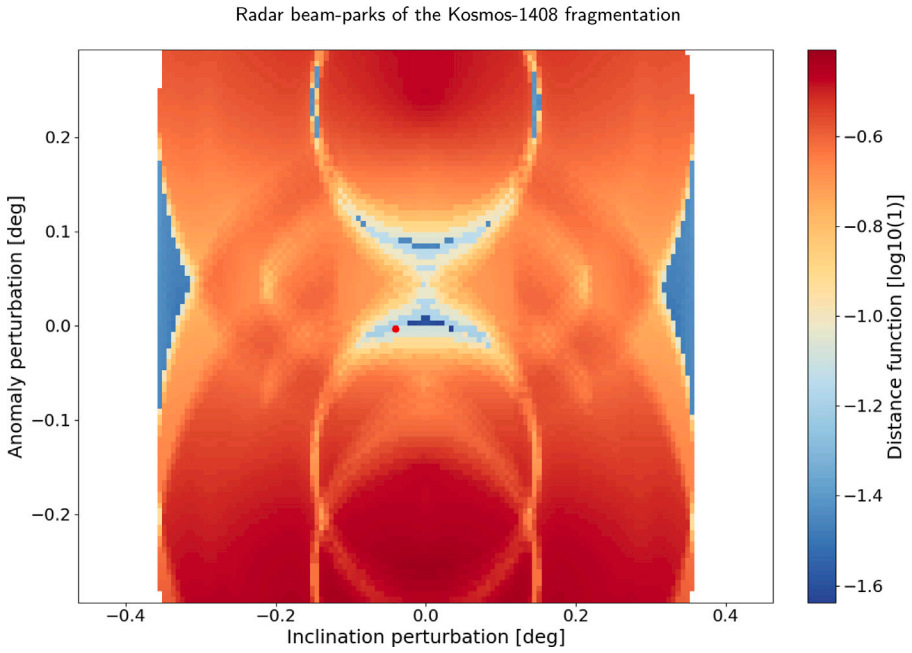

Fig. 4. The map of distance D as function of perturbations in inclination (δi) and mean anomaly ($\delta \nu$). The minimum point is marked with a red dot..

The assumption of circular orbits is a natural one when considering the natural dynamical evolution of objects in LEO [32,33]. Atmospheric drag perturbs eccentric orbits at their closest approach, lowering the altitude of the furthest approach, until they become close to circular. Given a circular orbit, detected range rate and inclination has a direct, although ambiguous, correlation. The ambiguity is limited to only two possible solutions however, whether the object was on an ascending or a descending track.

Due to this limitation a proper orbital element distribution cannot be estimated without *a priori* information. However, in the case of a debris cloud from a fragmentation event, we do have *a priori* information on the longitude of the ascending node.

We have used the Orekit[6] propagator to numerically propagate the original Kosmos-1408 orbit forward in time to our measurement points. This propagation provides us with a prediction of the longitude of ascending node of the debris cloud and allows us to disambiguate the circular orbit determination. The Orekit propagation was performed using a Dormand–Prince 853 integrator, included gravitational perturbations from the Moon and the Sun as well as a Holmes–Featherstone spherical harmonic expansion of orders 10 and 10 of the Earth gravitational field [34,35]. The DTM-2000 atmospheric model was used with F10.7 solar fluxes and Kp indices from NASA Marshall Solar Activity

[6] https://www.orekit.org/

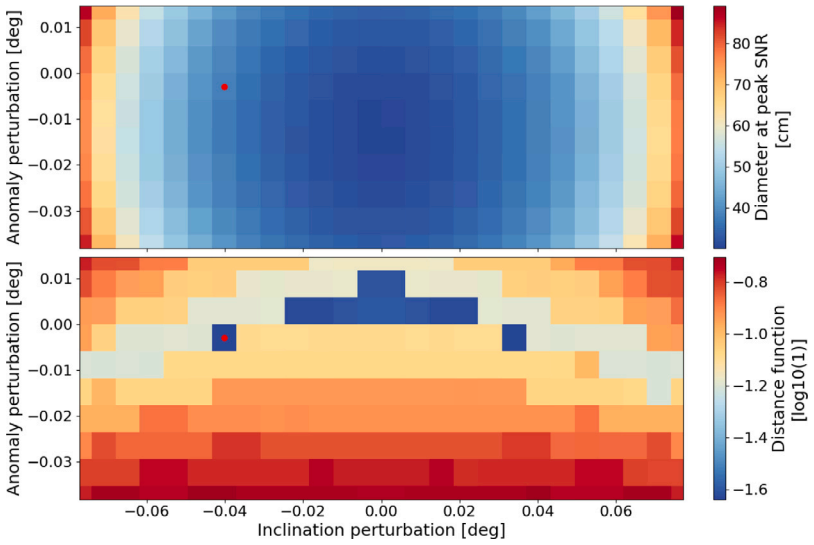

Fig. 5. The lower panel depicts the distance map in Fig. 4 but zoomed in on the region of best matches. The upper panel illustrates which object diameter is estimated for each proxy orbit that the map is a function of. The minimum distance point is marked with a red dot in both panels.

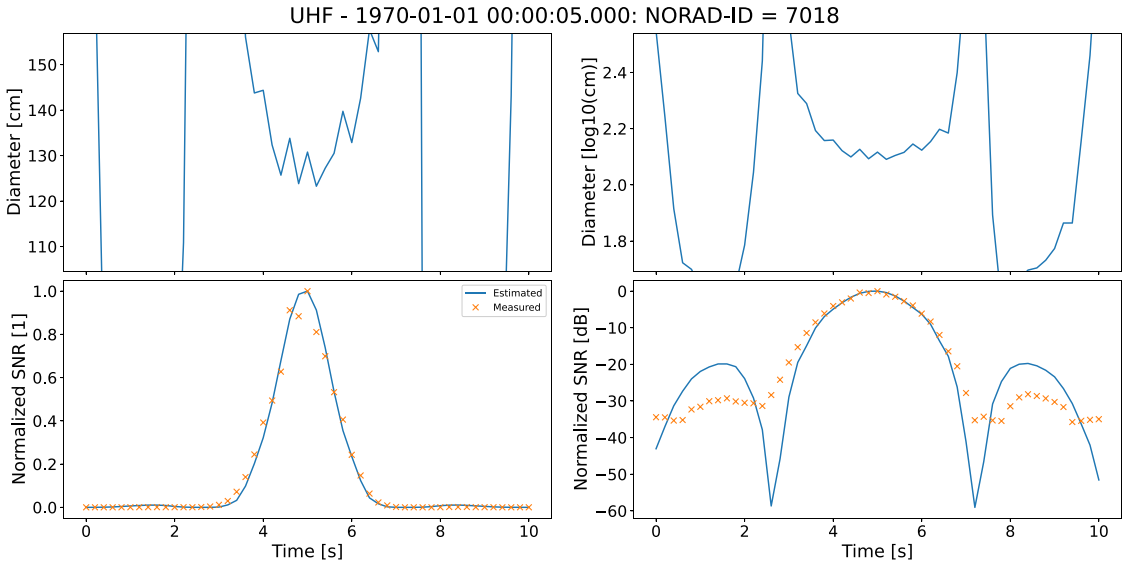

Fig. 6. Example matching of a measured SNR curve versus a simulated SNR curve and the resulting direct diameter calculation. This particular SNR curve was the best match out of all the proxy orbits simulated.

Future Estimation (MSAFE) and the solar activity set to weak [36]. The orbital evolution in True Equator, Mean Equinox (TEME) coordinates derived from the simulation is illustrated in Fig. 7.

3.6. Orbit determination

As was explored in the previous section, determining orbits from a single beam-park measurement does not provide that much useful information. It can inform on the statistics of the population but not much more than that. Rather, what one would like is to find the actual orbit of each individual object through orbit determination.

Performing orbit determination to update orbits with a known TLE prior is regularly and routinely done with all kinds of instrumentation to keep catalogues up to date. However, a subset of orbit determination is performing the IOD without a prior.

Performing an IOD is a much harder problem and usually requires more or specialized instrumentation, additional assumptions, or measurements over multiple orbits. IOD cannot be performed with only beam-park measurements without a priori information. However, as both the EISCAT UHF and the ESR performed measurements at the same time it is possible that the same object was detected in both beam-parks. Theoretically, two range and Doppler measurements at different places and times of an orbit is enough to perform an IOD. As such, we have here developed a method to test if dual-beam-park IOD is possible in practice.

In fragmentation events, the orbits of one or both of the colliding objects are usually known, and fragments tend to have orbits that are similar to these. Hence, radars can be pointed towards the passing debris cloud. As such, if it is feasible to perform IOD on such multi-beam-park measurements, it is a great asset to initial fragment cataloging. Even though it will be unknown which detections to match together, as a prediction exists on the time-frame of passage through the

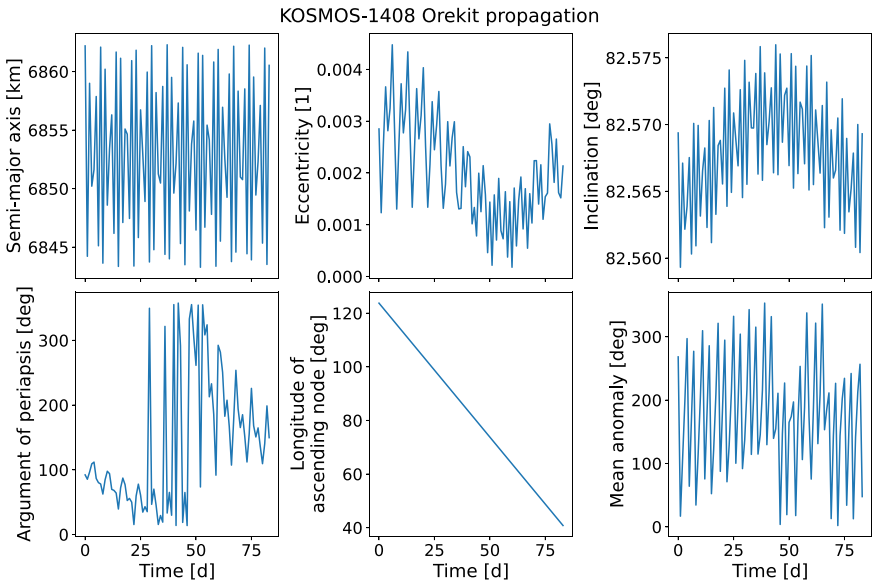

Fig. 7. Prediction of Kosmos-1408 orbital elements from the TLE epoch to the fragmentation event (2021-11-14 23:20:53). The propagation was made using the numerical propagator Orekit and the orbital elements shown are given in True Equator, Mean Equinox (TEME) coordinates.

beam, a quite reduced number of detections will have to be matched against each other.

To test the feasibility of this approach we have performed IOD on objects that are already known and were correlated in both measurement sets. These objects were identified by finding NORAD-IDs successfully correlated, using the method from Section 3.3, in both beam-parks. In the IOD, we do not use any information from the then known prior TLE and hence we have a reference to compare with.

As for the orbit determination itself, we have used a method based on the posterior $\mathcal{P}$ over possible orbital states $\mathbf{y}$. The posterior is defined by Bayes' theorem as

$$\mathcal{P}(\mathbf{y}) = \frac{L(D|\mathbf{y})\theta(\mathbf{y})}{\mathcal{P}(D)}, \tag{12}$$

where θ is the prior, L the likelihood, $\mathcal{P}(D)$ is a normalization constant, and D are the N number of measurements of the object. We denote conditional probability with |. The normalization constant, also commonly called the probability of the data, is defined as

$$\mathcal{P}(D) = \int L(D|\mathbf{y}')\theta(\mathbf{y}')\mathrm{d}\mathbf{y}'. \tag{13}$$

The likelihood itself is built from multiple Gaussians defined by the measurement errors σ_r(SNR) and σ_v(SNR). It is convenient to express this as the log-likelihood

$$\log_{10}(L(D|\mathbf{y})) = \log_{10}(C) - \frac{1}{2}\sum_{i=1}^{N}\left(\frac{r_i(\mathbf{y}) - \tilde{r}_i}{\sigma_r(\mathrm{SNR}_i)}\right)^2 + \left(\frac{v_i(\mathbf{y}) - \tilde{v}_i}{\sigma_v(\mathrm{SNR}_i)}\right)^2, \tag{14}$$

where the coefficient is

$$C = (2\pi)^{-N}\prod_{i=1}^{N}\left(\sigma_r(\mathrm{SNR}_i)\sigma_v(\mathrm{SNR}_i)\right)^{-1}. \tag{15}$$

To calculate the posterior we need to propagate the input state $\mathbf{y}$ to the measurement points. As such, it cannot be analytically evaluated and numerical methods need to be applied. We have implemented a three step IOD: first find a rough state estimate $\mathbf{y}$, then use an optimization method with that start value to find the peak of $\mathcal{P}(\mathbf{y})$, lastly use a Markov-Chain Monte-Carlo (MCMC) method to sample from the posterior to find the shape and mean of $\mathcal{P}(\mathbf{y})$.

We chose the mean elements used by the SGP4 propagator as the orbital state representation for our IOD methods [37].

To find the rough starting value we first attempt to solve the Lambert problem using two position vectors on the orbit separated in time. Assuming the target is in the center of the beam for both radars gives the two positions and the time difference needed. However, if this estimation fails, the backup method utilizes fitting a circular orbit to the two measurements. Again assuming the object is in the center of the beam, for one beam-park the possible circular orbit has one free variable as described in Section 4.2. By sampling this free variable we minimize the mean range and Doppler absolute residuals with respect to the measurements in the second beam-park of that circular orbit. The best orbit is then transferred into SGP4 mean elements and used as a start value for the coming step. The assumption that the target is in the center of the beam introduces an error on this initial estimation, with the Lambert problem being a lot more sensitive to this error than the circular orbit fit. However, we have not examined any quantitative impacts of such an error. It would depend on the orbit of the target and the observation geometry and this is outside the scope of this study.

We have not examined the updating of orbits in the current study. Therefore, we set the prior probability to uniform $\theta(\mathbf{y}) = 1$. When sampling the posterior we only need to sample a function that is proportional to the posterior so we can omit the constants C and $\mathcal{P}(D)$. As such, the likelihood defined in Eq. (14), without C, can be used as the posterior.

Given the Gaussian errors, the log of the likelihood, as defined in Eq. (14), becomes the negative of a least squares equation. As this equation can also be used as the log-posterior, we maximize the log-posterior using a Nelder–Mead optimization algorithm. We use the rough estimate from before as the start value for the Nelder–Mead algorithm, yielding the maximum *a posteriori* $\mathbf{y}_{\mathcal{P}\max}$ as a result [38].

Lastly, using $\mathbf{y}_{\mathcal{P}\max}$ as a start value we sample the posterior using the MCMC method known as Single Component Adaptive Metropolis–Hastings (SCAM) [39].

Generating the Markov-Chain is done through Monte-Carlo sampling of a so called proposal distribution and applying an acceptance probability. In SCAM this proposal distribution is a normal distribution. As such, its covariance matrix is commonly called the *proposal matrix*. We sample along the axis of the proposal matrix rather than the parameter axis of the problem to sample more efficiently. This ensures that the adaptive step-size of SCAM works well together with arbitrary proposal matrices.

However, sampling in mean element space using the SCAM method is not efficient as the Kepler space has inherently different topology than the Cartesian space. The measurement errors are defined as

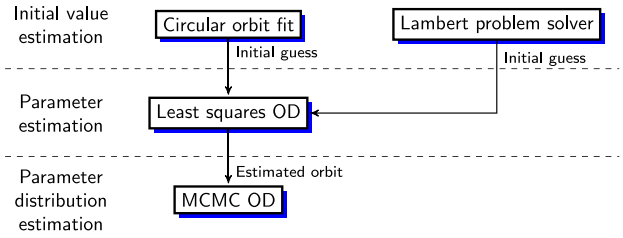

Fig. 8. Functional diagram of the IOD procedure. Here each function (boxes with shadows) use the measurements from both beamparks to refine the orbit. The Least squares OD uses the circular orbit fit initial guess if the Lambert problem solution orbit was hyperbolic.

Gaussian in Cartesian space; as such, the resulting posterior would be distorted in mean Kepler element space. To resolve this we simply transform the mean Kepler elements to mean Cartesian elements. This transform is using the standard Kepler transformation and is hence one-to-one and no adverse effects in sampling are introduced.

We also introduced two methods of determining the proposal matrix. First, we attempt to use linearized covariance estimations of the found maximum *a posteriori* to find the proposal matrix. The linearized covariance without a prior is defined as

$$\mathrm{cov}(\mathbf{y}_{p_{\max}}) = (\boldsymbol{J}^T \boldsymbol{\Sigma}^{-1} \boldsymbol{J})^{-1}, \tag{16}$$

where $\boldsymbol{J}$ is the Jacobian of the measurement simulation and $\boldsymbol{\Sigma}$ is the measurement error covariance matrix. If the linearization fails we instead start with the identity-matrix. We also omitted the standard 'burn-in' iterations usual in Bayesian applications as we already have an estimation of $\mathbf{y}_{p_{\max}}$ through the Nelder–Mead optimization [40].

The entire IOD procedure is illustrated as a functional diagram in Fig. 8. Generally, an IOD method can be split into three parts: initial value estimation, parameter estimation and parameter distribution estimation. The parts give, respectively, the start value for solving a non-linear problem that cannot be analytically evaluated, the solution of the non-linear problem and the estimated uncertainty of that solution.

We have chosen to apply an MCMC method to estimate the covariance of the posterior itself, rather than using a linearized estimation based on the numerically evaluated measurement Jacobean. Even though quite slow computationally in its current implementation compared to e.g. the Unscented Kalman Filter, this Bayesian method has the advantage of producing very precise information on the orbit determination covariance, even when it is non-Gaussian. Note the difference between the covariance of the maximum a posteriori estimation and the covariance of the posterior itself. Eq. (16) describes the former while the covariance of a set of MCMC samples describe the latter. However, when considering a linear model and Gaussian measurement errors these two coincide. Similarly, one should note that the maximum a posteriori coincides between the Nelder–Mead solution and the MCMC samples, while the maximum does not coincide with the mean if the distribution is asymmetric. Hence, we will report the maximum, mean, linearized covariance, and the MCMC sample covariance of the posterior.

An earlier version of the above described method has been used in simulations in Vierinen et al. [41] as well as with real data in Brändström et al. [42].

4. Results

We have only collected statistics on the observations performed in 2021 (cf. Table 1). These campaigns were performed soon after the event and in an early state of the debris cloud evolution. The observations in 2022 were performed as a follow-up study to enable investigating the long-term evolution of the Kosmos-1408 debris. As fragmentation modeling and hence also long-term propagation of realistic debris populations are outside the scope of the current study, the 2022 observations are only presented briefly. More detailed analysis of these data is left as future work.

Table 2
Summary of the limits of the 3d boxes used to select the possible Kosmos-1408 fragments. These limits were chosen based on density of detections compared to measurements of the space debris environment prior to the fragmentation, the predicted pass time of the Kosmos-1408 orbit and manual correction.

Radar	Start time [UT]	Selection limits		
		Time past start [hours]	Range [km]	Doppler [km/s]
UHF	2021-11-23 10:00	2.5–3	280–700	0.2–1.6
	2021-11-25 10:04	2.1–2.6	280–700	0.2–1.6
	2021-11-29 08:00	4.5–5.2	280–700	0.2–1.6
		19.2–19.8	280–700	−0.4–1
ESR(32)	2021-11-19 19:00	9.7–10.6	280–700	0.3–1.6
		16.6–17.6	280–700	0.3–1.6
	2021-11-23 10:00	2.4–2.75	280–700	0.2–1.6
ESR(42)	2021-11-25 10:04	1.65–1.8	280–700	0.2–1.6
	2021-11-29 08:19	2.75–3.2	280–700	0.2–1.6

4.1. Correlations

For the correlations we used two catalogues for each day with measurement campaigns. These two catalogues were created by taking the space-track snapshot of that day and separating out the Kosmos-1408 fragments from the rest. TLEs of the Kosmos-1408 fragments became public quite late and almost no data was available prior to the last 2021 campaign on the 29th. As such, we collected all TLEs available for these fragments in November and propagated them backwards to the observations for correlation rather than forwards as for the rest of the space-track catalogue. Examining the best matches for these correlations, the separation between the measurement time and the Kosmos-1408 fragment TLE epoch were sometimes more than a week. As such, the correlation results for the Kosmos-1408 fragment catalogue might not be reliable.

We also note that these correlations could have been more accurate if time-series data was used, as in the IOD and RCS analysis, instead of using the peak SNR data as was done here. With the current default data analysis procedure, only peak SNR data was saved for each individual event together with quick-look plots of the time series data, but not the numerical time series data itself. However, in the future if time series data of all events is stored by default, using such time series data with some data filtering should be the preferred correlation method.

The correlation results were grouped into four categories. The statistics for each category is given in Table 1. These categories are

- Correlated
  - Kosmos-1408 fragments
  - Background RSO's
- Uncorrelated
  - Possible Kosmos-1408 fragments
  - Background RSO's

The category of Possible Kosmos-1408 fragments were selected based on a 3d box in time, range and Doppler consistent with the debris cloud. Ideally, large statistical fragmentation simulations together with fragment propagation and measurement simulation should inform the selection region. However, as such simulations are outside the scope of this study, we instead use one static 3d-selection region for each campaign. The limits are based on the density of detections compared to measurements of the space debris environment prior to

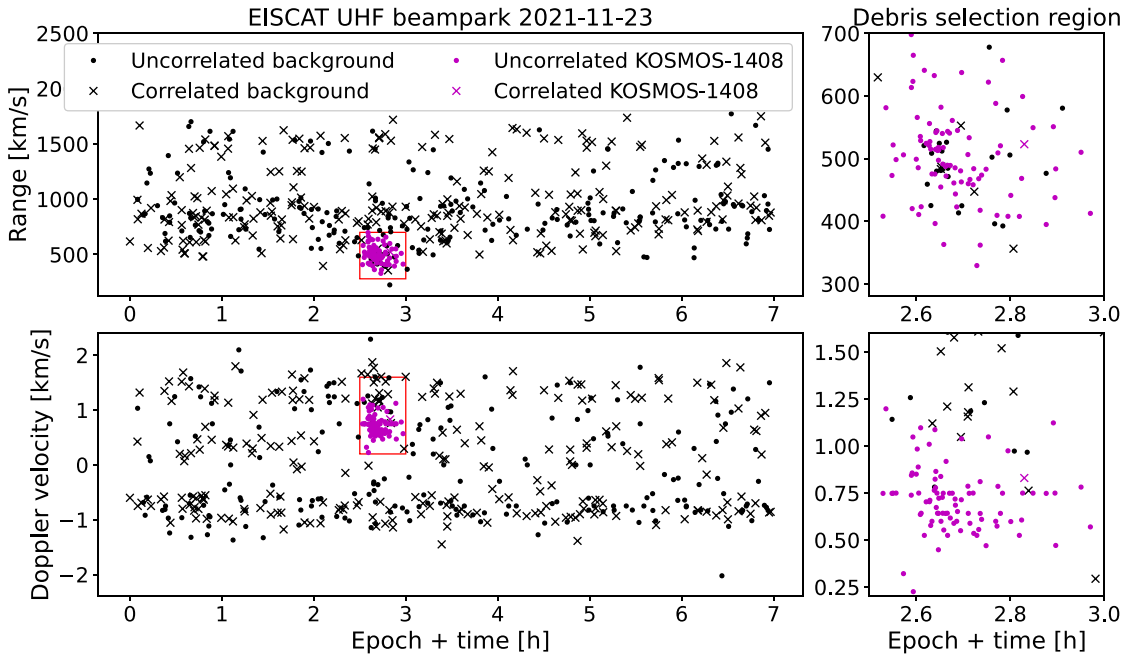

Fig. 9. Detected events during the 2021-11-23 EISCAT UHF campaign, categorized according to the correlation results and selection of the Kosmos-1408 debris cloud. The right panels are zoomed in regions of the selection region.

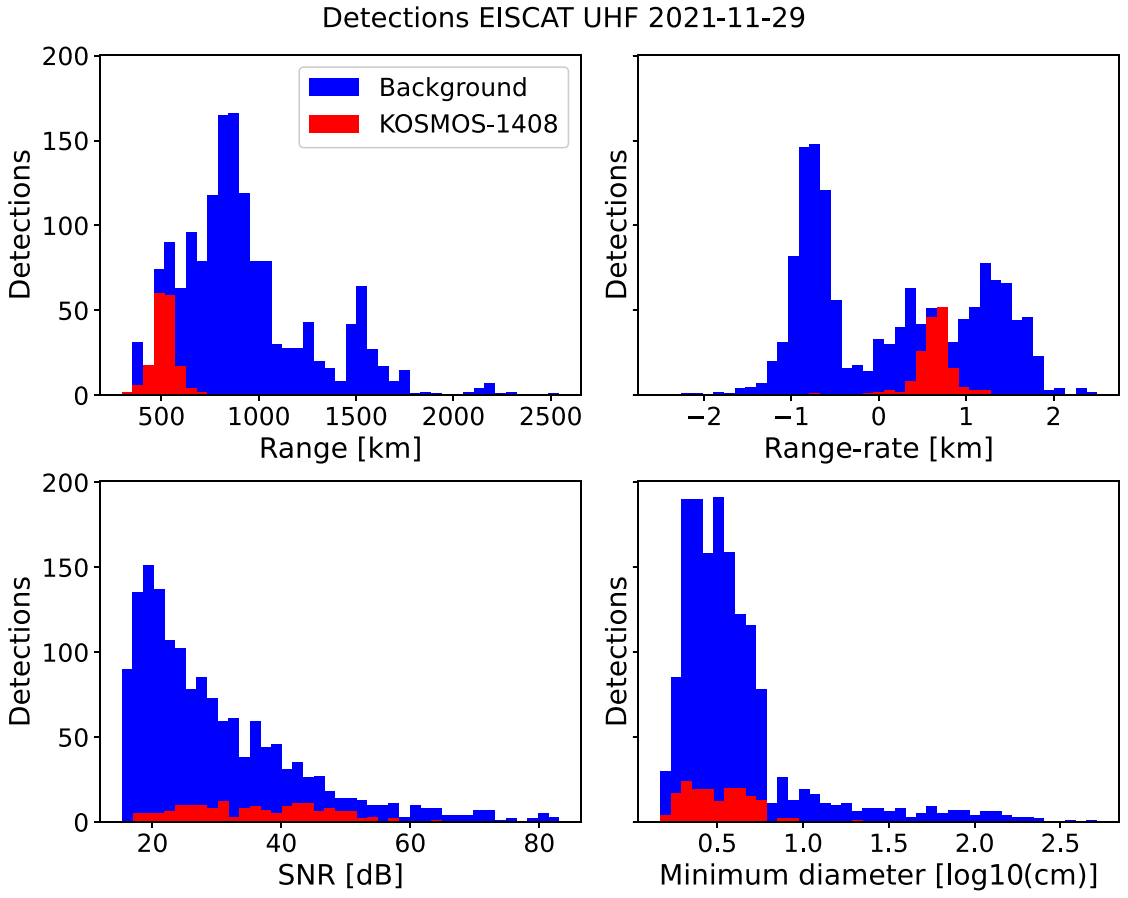

Fig. 10. Kosmos-1408 and background debris stats.

the fragmentation, the predicted pass time of the Kosmos-1408 orbit and manual correction of the limits. The selection limits are listed in Table 2. An example of this selection, the first row of Table 2, as well as the resulting categorization of one campaign is illustrated in Fig. 9. Here uncorrelated results are represented as dots while correlated results are represented as crosses. Kosmos-1408 fragments

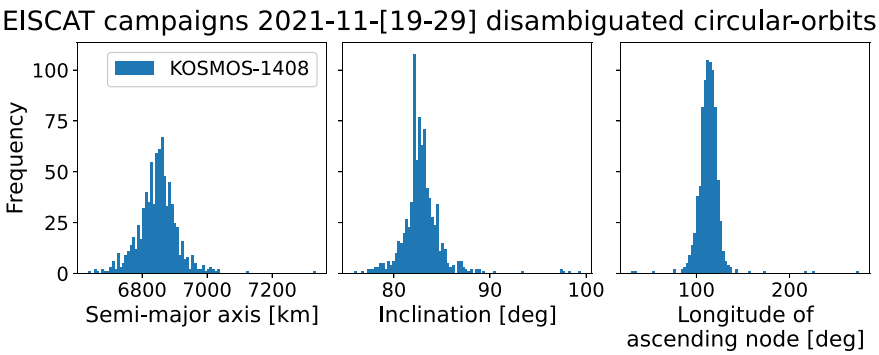

Fig. 11. Distribution of estimated circular orbits of the possible Kosmos-1408 fragments detected during all 2021 campaigns. The orbits are disambiguated using the Longitude of ascending node predictions.

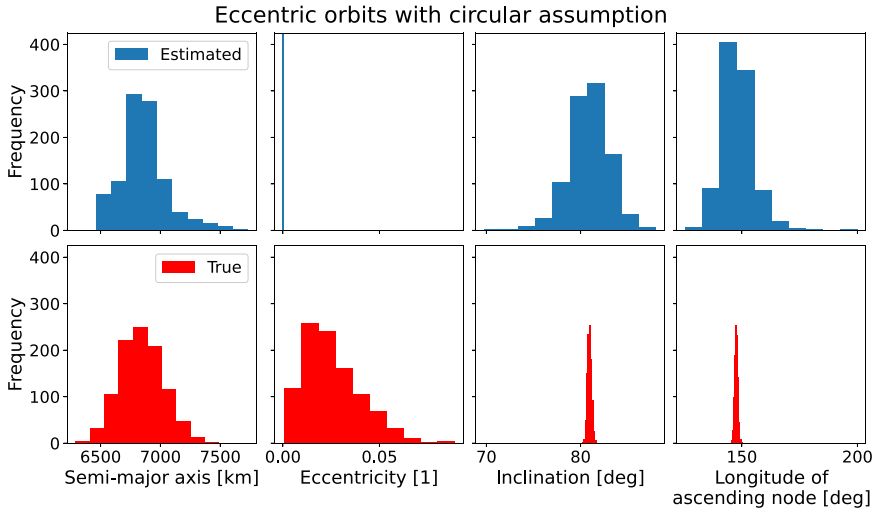

Fig. 12. Simulated circular orbit distribution calculated but from detections of a distribution of non-circular orbits. The top row depicts the estimated distribution and the bottom row depicts the input true distribution of orbits.

are colored magenta and the rest are black. The red regions denote the 3d-selection regions and the right hand column shows a close-up of the detections in the selection regions. The UHF measurements contain a lot more uncorrelated results than the ESR measurements (cf. Table 1). The reason for this is that the UHF is a more sensitive system than the ESR and probes objects of smaller sizes.

In the following, we use "Kosmos-1408" to refer to all detections categorized as correlated or uncorrelated Kosmos-1408 fragments. For example see Fig. 10, where the measured parameter statistics are illustrated for one of the campaigns.

4.2. Circular orbit determination

Applying the assumption of a circular orbit and the disambiguation of the results using the predicted Kosmos-1408 longitude of ascending node precession, as described in Section 3.5, we calculate a circular orbit distribution based on all detections from the 2021 campaigns. This distribution is illustrated in Fig. 11. During these 10 days the longitude of the ascending node is predicted to drift a few degrees and will widen the distribution shown here.

Due to the limitations of the circular assumption, we can put this orbit distribution into context by simulating the measurements of a simple, non-circular, orbit distribution and then applying the circular orbit determination on these simulated measurements. We generated an orbit distribution by applying a 3d symmetric normal distribution, with standard deviation $\sigma = 100$ m/s, to perturb the velocity of a circular orbit. The true orbit distribution as well as the estimated circular orbit distribution is illustrated in Fig. 12. The simulated orbits also had randomized argument of periapsis which induced a spread in estimated semi-major axis distribution. This deviation also introduced a non-perfect alignment with the measurement point and bore-sight, introducing an additional distribution spread. The example illustrates that even though a velocity perturbation affects the inclination and the longitude of the ascending node, the majority of the spread in these estimated circular orbit distributions can stem from the eccentricity distribution.

4.3. Size estimation

Individual object size-estimation based solely on beam-park data is a novel approach that required substantial testing and development. Therefore, we did not apply the analysis to the entire observational data-set. Instead we chose one specific hour from the UHF 2021-11-23 campaign during the passage of the Kosmos-1408 debris cloud. This allowed an attempt at characterizing the debris cloud size distribution from a single monostatic measurement while at the same time providing enough correlated background as validation material.

We performed two versions of the analysis, one where the full gain pattern was used and one where the gain pattern was truncated at 1.8° half width from boresight. We tried both methods since the model may be quite unreliable further away from boresight than that. In the end, the results were significantly better for the truncated model; as such, we only present those results here. For radar observations with better characterized far-out side-lobe structures, this approach will perform better without truncating the gain model.

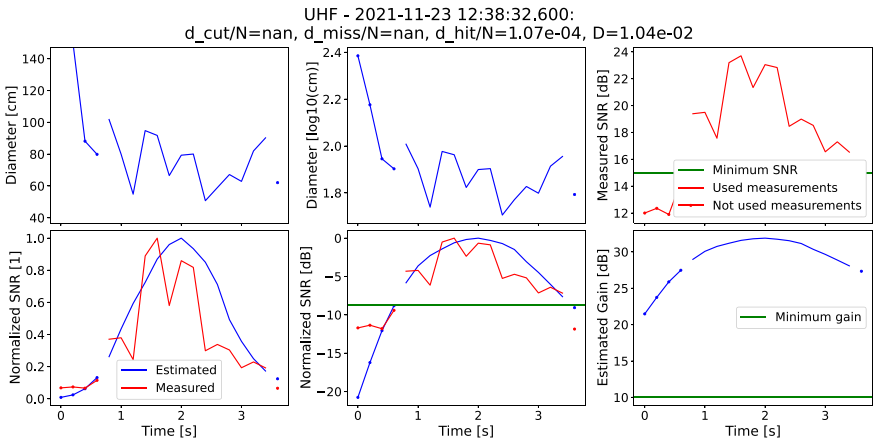

Fig. 13. Example diameter estimation of a target with oscillating RCS, probably due to the rotation state of the object. Illustrated is the best matching of the measured SNR curve versus the simulated SNR curve and the resulting direct diameter calculation.

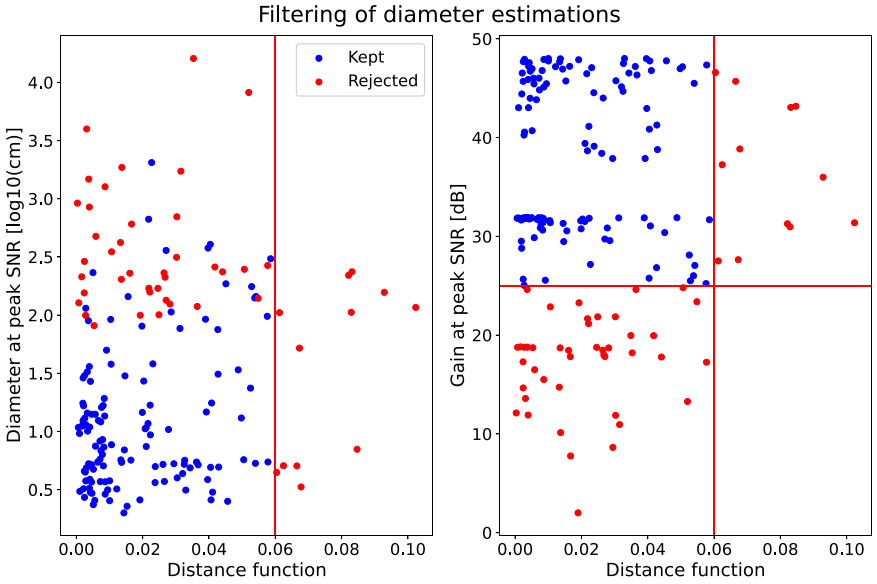

Fig. 14. Filtering of size estimation results to remove potentially failed estimations. The two panels illustrate two planar projections of the three dimensional data-set. The red lines denote the limits (minimum gain at peak SNR and maximum distance function value) used for discarding individual size estimations. As the same data set is illustrated in both panels, but displaying different parameters on the y-axis, the rejected points in the left panel below the distance function limit are rejected due to being below the gain-limit, as illustrated in the right panel.

As we mentioned previously, this method does not account for oscillating RCS due to e.g. rotations of the object. However, when examining the data we do detect several objects that exhibit this behavior. One such example is illustrated in Fig. 13. Calculating the distance function in decibel space rather than linear space, given that the period of oscillation is faster than the passage through the gain pattern, the matching algorithm will still manage to find reasonable results. However, if the oscillation rate is on the same rate as the passage through the gain pattern, "false" lobe structures may be created and possible faulty matches may be made.

We know that the gain model is not perfect and that the assumption of constant RCS does not always hold. We can, therefore, assume that a portion of the estimation attempts will not succeed. As such, we need to filter the results before compiling meaningful statistics. We chose to do this based on the found minimum distance D as well as the simulated gain at peak SNR. The limiting value of 25 dB gain was chosen based on the side-lobe at $\sim 2.5°$ off-axis angle, which is the largest side-lobe that can be considered not well characterized. If the peak SNR is located at or below this gain value, then the object stayed exclusively in regions of the gain pattern that are not well defined and we do not want to include it in the resulting statistics. The distance D is normalized according to the number of points in the time-series to allow comparison of individual minimum-distances. We assume the outlying percentage of minimum-distances D indicates a bad match compared to the typical case. All events with $D > 0.06$ are considered as outliers and are removed from the results. This filtering is illustrated in Fig. 14. The limits are here illustrated by the red lines cutting through the distribution.

The remaining statistics in terms of estimated diameter as well as estimated off-axis angle are illustrated in Figs. 15 and 16 respectively. We can here see from Fig. 16 that most detections are made inside the main lobe but a comparable amount is also done in the first sidelobe. For comparison, we can refer to the minimum possible diameter estimation based on assuming the object is in bore-sight as illustrated in Fig. 17.

Comparing the size distribution estimated in Fig. 15, the background population distribution is consistent within a factor of two with current state of the art debris models. As a reference we simulated one hour of measurement time using the EISCAT UHF in the same configuration as the campaign here. The population used was the MASTER

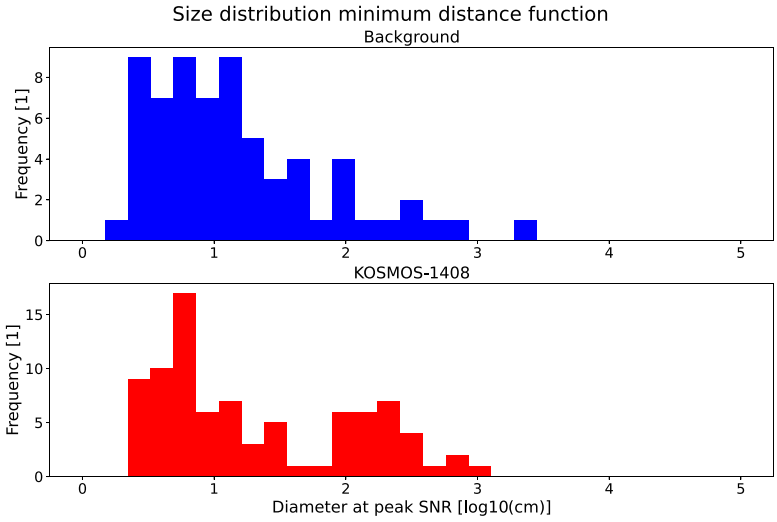

Fig. 15. Estimated size distribution, after filtering, between 12:00 and 13:00 during the 2021-11-23 EISCAT UHF beam-park campaign. The possible Kosmos-1408 fragments were separated from the rest using the results outlined in Section 4.1.

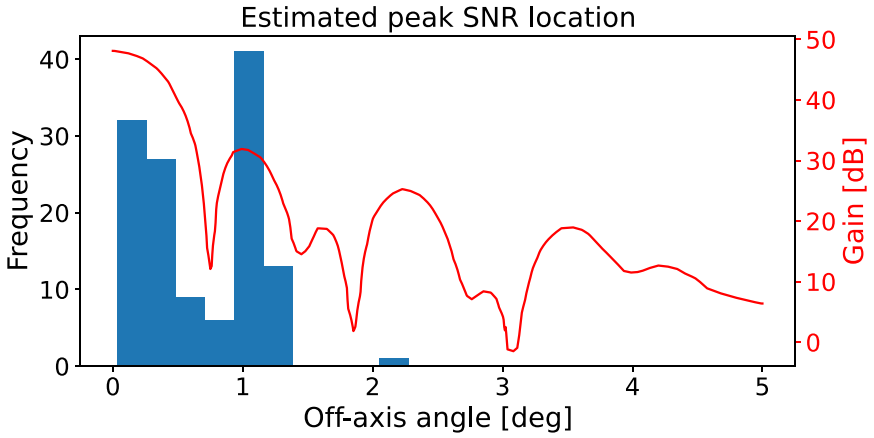

Fig. 16. Prevalence of off-axis angle corresponding to maximum SNR, plotted together with radially symmetric gain.

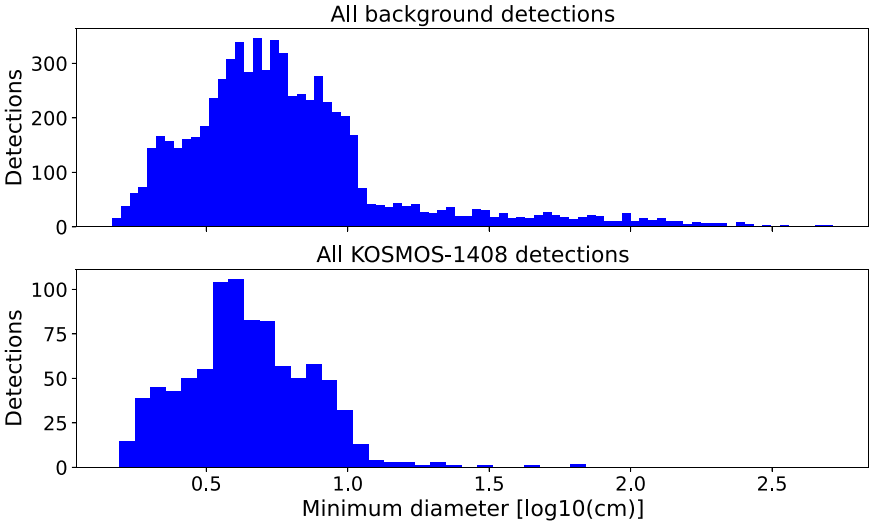

Fig. 17. Minimum diameter estimation of all events detected during the 2021 beam-park campaigns with both the UHF and ESR systems. The possible and correlated Kosmos-1408 fragments were separated from the rest using the results outlined in Section 4.1.

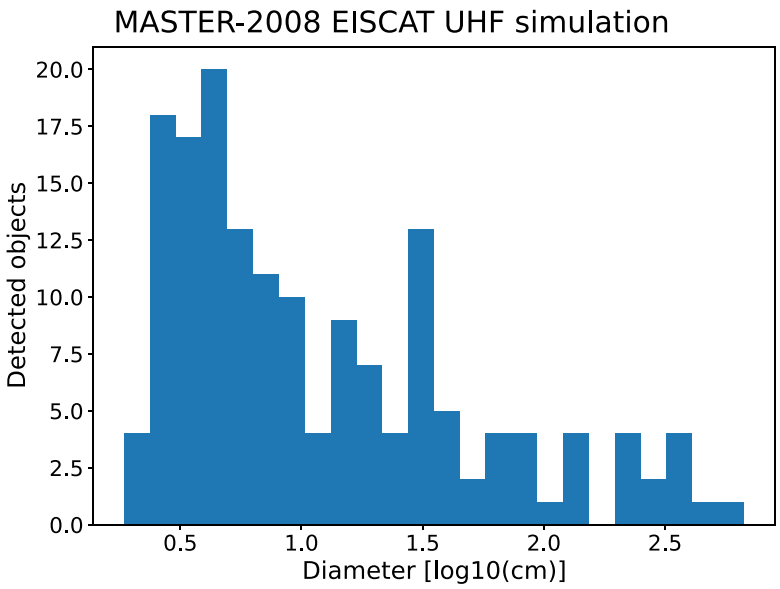

Fig. 18. Size distribution of detected objects in a 1 h simulation of the EISCAT UHF observing the MASTER 2008 population, limited at 1 mm diameter.

2008 debris population model with a size threshold of 1 mm diameter. The predicted distribution of detected sizes is illustrated in Fig. 18. The only significant difference between the estimated distribution in Fig. 15 and the simulated distribution in Fig. 18 is a larger amount of small objects in the MASTER simulation as well as an overall lower detection rate in the measurement. The lower number of detections can be accounted for through missed detections in the analysis software. We also applied filtering for only good matches towards the measured SNR curve so that e.g. objects with large RCS oscillations would be discarded. The same is true for the signal analysis where a number of effects can discard events that is not accounted for in the MASTER simulation in Fig. 18, e.g. removal of low SNR detections where range was determined but Doppler could not be.

Examining the estimated size distribution of the Kosmos-1408 fragments in Fig. 15, a portion of the very largest sizes are probably miss-classified detections or failing estimations. However, there is a secondary peak at $\sim$ 1 m diameter objects. A size of 1750 kg can theoretically produce a large number of debris with significant surface area for this second peak to be real. Radar surveys to discover and track the fragments from Kosmos-1408 by the private enterprise LeoLabs have also indicated several large objects, which have been attributed as potentially being parts of solar panels and other large structural elements,[7] from the destroyed satellite. More in depth fragmentation modeling is needed to put these results into context and determine whether this estimated distribution is generated by the actual population or failed size estimation attempts, such as ambiguities in the SNR curve matching.

As validation of the technique we selected all correlated events within this hour and predicted the path through the gain pattern using the TLE. This predicted path was used to estimate the size of the object. The sizes of these objects were also estimated using the SNR curve matching method. Fig. 19 illustrates the comparison between size estimations based on the predicted TLE trajectory and the size estimations based on the SNR curve matching. If the TLE prediction is accurate, we can assume that the size estimations from the TLE are fairly accurate as well. The rightmost panel of Fig. 19 illustrates that size estimations from SNR curve matching are almost always on the same order of magnitude as the ones from the TLE predictions. This serves as a positive validation of the technique. However, there is a slight skew to larger sizes in estimations using the SNR curves. This is probably due to the gain model not being sufficiently accurate or due to ambiguities in the SNR curve matching.

Table 3
Residuals from comparing the Least squares Nelder–Mead IOD to the beam-park measurements. The time difference column denotes the absolute time between the detection in the UHF and the ESR beam-parks.

IOD versus measurement absolute residuals					
NORAD-ID	Mean range residuals [km]		Mean Doppler residuals [km/s]		Time difference [min]
	UHF	ESR	UHF	ESR	
703	0.075	0.074	0.009	0.017	2.6
4331	0.087	0.108	0.322	0.098	97.6
4394	0.066	1.212	0.009	0.594	96.8
15938	0.054	0.045	0.024	0.032	2.6
20565	0.197	0.344	0.216	0.541	2.3
21284	0.069	0.093	0.009	0.019	104.9
25759	0.070	0.044	0.010	0.020	96.2
29840	0.079	1.061	0.005	0.493	94.8
41336	0.065	0.817	0.008	0.147	93.0
43476	0.068	0.168	0.021	0.240	2.3
43477	0.069	0.219	0.031	0.169	2.3
43656	0.138	0.354	0.047	0.192	97.7

4.4. Orbit determination

Initially, our intention was to point the radar systems, during the 2022 follow up campaign, in a configuration specifically for Kosmos-1408 fragment IOD. Such a pointing would allow the fragment cloud would pass through the main lobe of one system and subsequently through the other system's main lobe within the period of one orbit. However, the UHF radar experienced a phase-stability problem prior to the campaign and the gearbox for the steerable ESR antenna was broken at the time. As such, we chose to use the previously used pointing direction for the UHF in order to have comparable measurements in case the phase-stability problem persisted.

Instead, the data from the 2021-11-23 campaigns at UHF and ESR(32) were reanalyzed to store numerical time-series data for all individual detected events, to enable applying the IOD technique test on correlations from this day. During these two campaigns there were a total of 12 objects correlated successfully in both beam-parks.

[7] https://leolabs-space.medium.com/part-iii-cosmos-1408-breakup-observations-one-month-later-1f7eb0955172 accessed 2022-05-24

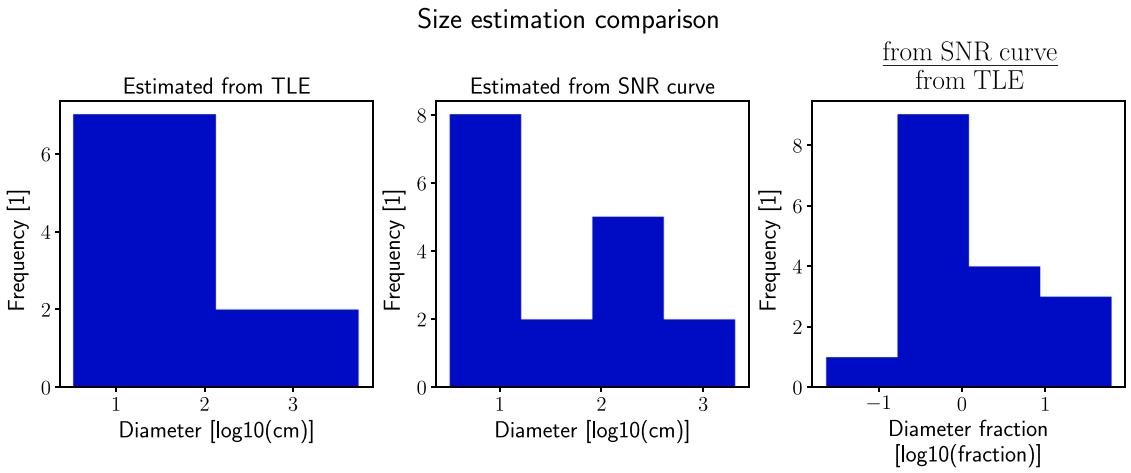

Fig. 19. The leftmost panel shows size estimation based on the trajectory from TLE predictions. The middle panel shows the size estimations for the same objects but using the SNR curve matching method. The rightmost panel shows the fraction between the two estimates for each individual object.

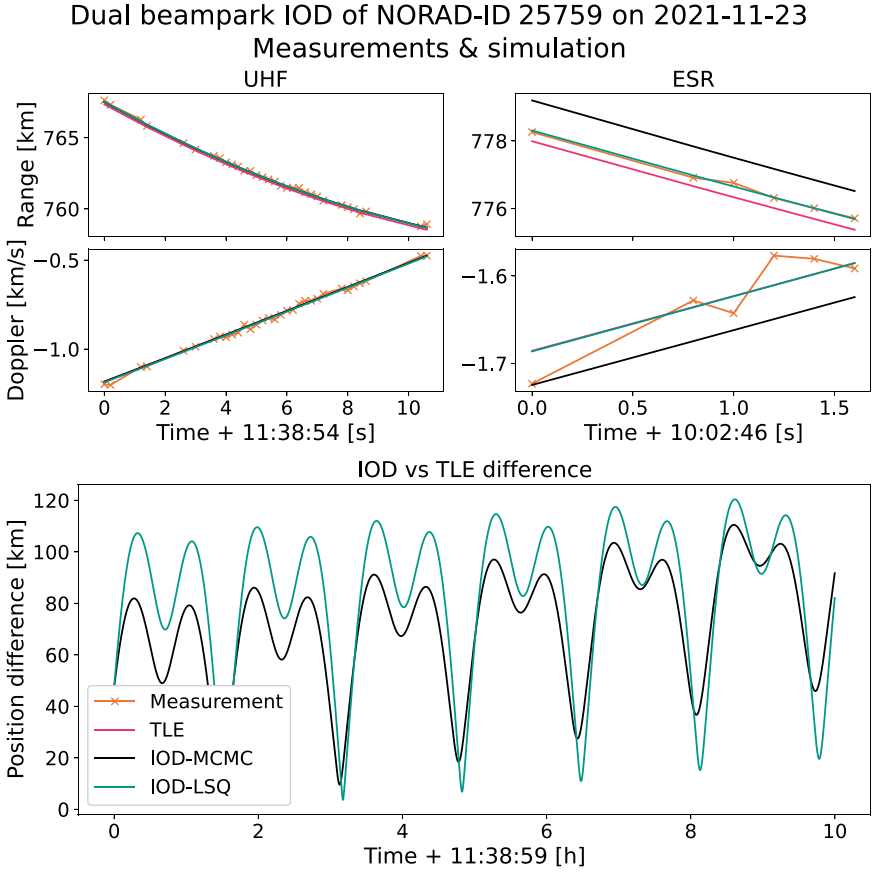

Fig. 20. Measurements and IOD results for NORAD-ID 25759 detected in two consecutive beam-park experiments together with the position difference between the IOD and the TLE as a function of time.

As an example, the IOD of NORAD-ID 25759 is illustrated in Fig. 20. The top four panels depict the simulated range and Doppler velocities in the two beam-parks for the three different orbital states. These three states are the maximum a posteriori labeled IOD-LSQ (LSQ being shorthand for Least Squares), the mean a posteriori as calculated from the MCMC samples labeled IOD-MCMC and finally the correlated TLE itself. These predictions are illustrated together with the actual measurements made by the radars for comparison.

The lower panel of Fig. 20 shows the position difference as a function of time between the two IOD orbits and the TLE orbit. Unfortunately we do not know the quality of the TLE. This means that the positional difference is not only due to the error in the IOD, but it also includes errors in the original TLE. However, assuming that the original TLE is of higher quality than our IOD, the error is an indication of how well the IOD can be used to schedule followup observations. For this particular example the oscillations are only slowly growing and would

Table 4
Absolute difference between the mean elements outputted from the IOD and the mean elements from the correlated TLE.

IOD Mean elements versus TLE absolute difference								
NORAD-ID	Least squares Nelder–Mead				Mean Posterior MCMC			
	a [km]	e [1]	inc [°]	RAAN [°]	a [km]	e [1]	inc [°]	RAAN [°]
703	19.409	0.002	0.339	0.304	32.754	0.002	0.628	0.474
4331	4.940	0.006	1.010	0.329	3.767	0.004	1.210	0.275
4394	1.889	0.004	1.281	2.281	1.542	0.002	1.097	2.845
15938	110.718	0.017	1.525	3.439	17.933	0.004	0.784	1.468
20565	18.140	0.006	1.406	1.869	127.477	0.010	1.218	1.352
21284	0.607	0.008	1.026	3.206	1.025	0.008	1.065	3.322
25759	0.503	0.003	0.577	0.544	1.012	0.002	0.509	0.343
29840	2.335	0.009	0.826	2.933	2.532	0.009	0.818	2.911
41336	3.586	0.022	4.784	3.372	3.744	0.021	4.800	3.326
43476	0.833	0.002	0.837	1.190	48.706	0.005	0.601	0.527
43477	1.502	0.002	0.771	1.064	11.482	0.000	0.500	0.349
43656	5.144	0.021	2.947	9.285	2.661	0.018	3.164	9.900

allow scheduling followup observations. For comparison, the main lobe full width half max (FWHM) of the UHF and ESR are ∼8.6 km and ∼26.9 km respectively at 700 km range. So at the largest positional difference a substantial search grid would be needed to reacquire the target, while at the smallest one a single pointing direction would suffice.

Around half of the IOD results had a much more rapid divergence or much larger oscillations than the example in Fig. 20. A more detailed study would be needed to determine if they are useful for followup observations. The other half can preliminary be said to be useful for reacquiring the object. The results from all analyzed events are summarized in Tables 3–5. In Tables 4 and 5 we omit the argument of perigee and mean anomaly as these are not very informative for near circular orbits.

From the *Time difference* column of Table 3 we can note that all double beam-park detected objects were either detected on the same orbit or on subsequent orbital passes. From the mean range and Doppler residuals we also notice that all the IODs produced states that fit quite well with the measurements.

Table 4 compares these two IOD mean element states with the correlated TLE mean elements. Generally the IOD produces small differences to the TLE indicating that this method is practically viable to assist with initial cataloging of e.g. a fragmentation event. Similarly the standard deviations of the MCMC samples of the posterior is listed in Table 5. However, the covariance of these samples are not diagonal and many are also non-Gaussian in shape, partly due to orbital dynamics introducing non-linearity in the posterior due to propagation. As such, these standard deviations are slight over-estimations of the actual mean element uncertainty. However, in Table 5 we also list the estimated covariance using linearization. The non-linearity of the dual beampark IOD is further exemplified by the very large standard deviation when estimating a linearized covariance. Due to possible non-Gaussian distributions, the mean a posteriori is probably not a useful method for determining a representative orbit, rather the maximum a posteriori should be used if one absolutely needs a single representative orbit rather than the distribution itself. In this case, the MCMC samples should be used to estimate the posterior probability distribution function and, if applicable, its covariance.

An interesting observation is that all of the worst orbit determinations in Tables 4 and 5 are objects with a time difference in Table 3 of ∼2 min, i.e. detection on the same orbit. This makes sense as there is more dynamical information in two measurements when they are separated by an entire orbital period. At the same time this separation does not introduce too much non-linearity from propagation to make the posterior difficult to evaluate.

4.5. Follow up observations

Having long term observations of a debris cloud can reveal information about the statistical properties of the debris, which in turn inform about the fragmentation parameters. We performed a final follow up observation approximately 5 months after the destruction of Kosmos-1408. The detected events during these campaigns are illustrated in Figs. 21 and 22 for the EISCAT UHF and ESR respectively. The cloud itself is still visible at ∼19:00 and ∼10:00 UTC in Fig. 21 and at ∼19:00 and ∼11:00 UTC in Figs. 22.

We did not run any further analysis on the followup observations. However, as the cloud is still visible, this data can be used in followup studies on fragmentation modeling.

5. Discussion

Starting off with the circular orbit distribution estimation in Section 4.2: from fragmentation modeling we know that fragments originally are perturbed in eccentricity and semi-major axis and many orbits will not circularize quickly. Hence, the distribution in Fig. 11 is quite misleading. We believe that the best way to derive orbit distribution information from a debris cloud like this is to perform a generalized density estimation through solving an inverse problem. Then, appropriate variables can be fixed or set to particular distributions when generating the basis observation density functions used in the inversion. For example, the measurements might contain enough information to infer an unknown parameter in a fragmentation model. However, such generalized density inversion is outside the current scope and left as future work.

A much more promising technique is the size estimation method through SNR curve matching presented in Section 4.3. Firstly, the method was successfully validated against catalogued objects. Even though the errors are still large, the improvement is significant compared to just providing a lower size limit.

Looking at the distribution in Fig. 15, it should be noted that LeoLabs has reported observing less small debris than expected[8] and several pieces of large debris in the cloud, as previously mentioned. This is consistent with our estimation of the size distribution and that the debris cloud was still clearly visible in the followup observations (Figs. 21 and 22). Given that the group of debris still persists as a tight enough cluster to be visible in a beam-park needs to be compared with simulations to make firm conclusions. However, without such simulation, we can speculate that either the initial velocity perturbations were smaller than regular explosion events or that the initial size distribution contained a population of larger fragments that are less perturbed, or a combination of both. This is not consistent with a hypervelocity impact. An impact can be considered hypervelocity if the relative velocity between the two bodies exceed the speed of sound in solid material, i.e. ≈ 4–5 km/s.

Since this method proved useful we will in the future work apply the size estimation technique to the entire data-set available.

Moving on to the multi-beam-park IOD feasibility test described in Section 4.4: unfortunately, no measurements pointing both radars straight at the debris cloud were made during the campaigns. Hence, we resorted to testing the technique on catalogued objects as a proof-of-concept. Fortunately, as this test indicates the technique as feasible and it might inform future campaigns of similar events.

Additionally, there are ongoing projects to examine the possibility of re-purposing the EISCAT VHF facility into a 4-panel beam-park Space Debris radar with a linear phased array along the feed-bridge [43]. The proposed system is called Tromsø Space Debris Radar (TSDR) and would be able to detect many objects in two or more of the monostatic

[8] https://leolabs-space.medium.com/part-ii-new-observations-on-cosmos-1408-breakup-3d8e5441f720, accessed 2022-05-24

Table 5
Standard deviation of the MCMC samples of each state variable and standard deviation using a linearized covariance of the maximum a posteriori parameter estimation. It should be noted that the variables here are sometimes highly correlated as well as non-Gaussian so these standard deviations are not fully representative of the error, especially the linearized covariance estimate as it is a quite rough approximation.

NORAD-ID	MCMC IOD mean elements standard deviation				Linearized covariance estimate			
	a-std [km]	e-std [1]	inc-std [°]	RAAN-std [°]	a-std [km]	e-std [1]	inc-std [°]	RAAN-std [°]
703	26.577	0.004	0.427	1.146	87752	0.277	0.368	1.005
4331	0.171	0.000	0.091	0.277	90408	0.267	0.292	0.947
4394	0.067	0.001	0.115	0.350	551502	0.294	0.121	0.475
15938	24.926	0.003	0.317	0.843	249619	0.288	0.317	1.048
20565	16.822	0.002	0.220	0.571	213509	0.284	0.372	0.441
21284	0.246	0.000	0.137	0.411	771618	0.281	0.207	0.478
25759	0.246	0.003	0.285	0.843	400968	0.282	0.156	0.411
29840	0.120	0.001	0.091	0.282	193214	0.289	0.133	0.477
41336	0.115	0.001	0.067	0.198	3480	0.132	0.055	0.276
43476	10.423	0.002	0.255	0.674	70032	0.229	0.167	0.388
43477	6.602	0.002	0.361	0.947	16009	0.171	0.257	0.243
43656	0.401	0.001	0.052	0.146	103334	0.288	0.134	0.477

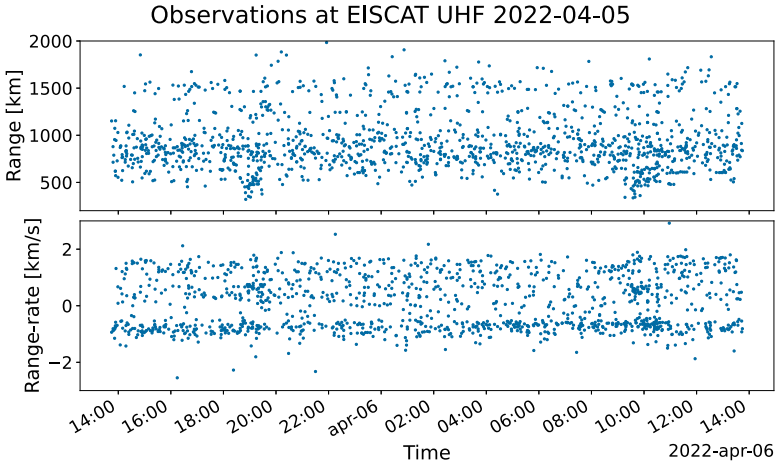

Fig. 21. Follow up observations of the debris cloud with the EISCAT UHF radar ~5 months after the fragmentation event.

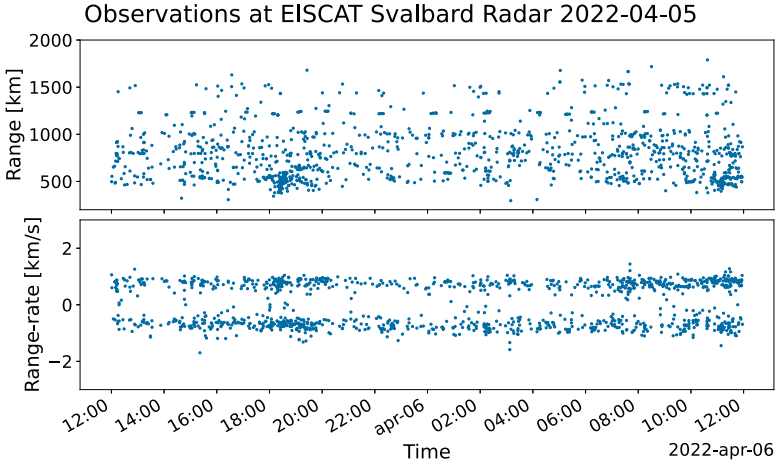

Fig. 22. Follow up observations of the debris cloud with the EISCAT Svalbard 42 m radar ~5 months after the fragmentation event.

fences produced by the phased feed-bridge. Performing an IOD with this system would be similar to performing it on the multi-beam-park measurements we have performed here. Hence, this proof-of-concept supports the design process of the TSDR system.

If an IOD pipeline based on the method presented here is to be built, there are some significant improvements that can be made. Firstly, the calculation of the start value, using either the Lambert problem or the circular assumption, is quite crude and unreliable and can surely be improved upon, e.g. as done in Christian and Parker [44] for bearing and range rate as variables. Secondly, we did not implement realistic uncertainties σ_r and σ_v but instead simply fixed these to typical values. Such an improvement would generate a more realistic posterior sample distribution. Additionally, a higher resolution data analysis to find the range and Doppler of the targets should be used to reduce any algorithmic biases from the measurement data.

Finally we note that the time-offset used in correlation, as described in Section 4.1, could have been a lot finer. We recommend a step size close to the coherent integration time cycle, here 0.2 s, which would

have resulted in 51 samples instead of 11. Fortunately the results were not negatively affected by this lower resolution for this analysis.

6. Conclusions

We have presented multiple beam-park observations of the Kosmos-1408 debris generated by the intentional destruction of the satellite. Seven of the campaigns (on four separate days) were within 14 days of the fragmentation event and two followup campaigns were conducted approximately 4 months after the last campaign to observe the long term evolution of the debris. The summary of the campaigns is listed in Table 1. These observations were used to select and discriminate known and previously unknown fragments of Kosmos-1408. This selection of fragments were then processed further.

Inclination and semi-major axis distributions were computed using a circular orbit assumption. These distributions proved not useful due to the circular orbit assumption. Instead we proposed a more generalized density inversion technique to determine parameters of interest while incorporating as much a priori information as possible.

We also applied a novel size estimation technique using SNR curve matching applied on one hour of data from the 2021-11-23 UHF campaign. The technique proved powerful enough to produce accurate size estimates on the validation population of catalogue objects. The technique was used to produce a size distribution estimate for the Kosmos-1408 fragments as well as detections not associated to Kosmos-1408. This estimated size distribution is illustrated in Fig. 15. The distribution agrees with previous estimates on the type of impact that lead to the fragmentation of the satellite. The background distribution also agrees with theoretical predictions.

We also performed IOD using two simultaneous beam-parks at different geographical locations not pointing to a common volume. Although we could not apply the technique on the Kosmos-1408 debris cloud due to technical issues in relation to the campaign, we applied it on catalogued objects detected during the campaigns as a proof-of-concept. The results indicate that this can be a useful technique to use after a recent fragmentation event. By pointing two or more beam-parks at the expected orbit of the debris cloud, a similar IOD method as outlined here can be applied. If the objects can be separated from each other in the data, a few such campaigns could quickly catalogue a significant portion of fragments. However, keeping the objects in a catalogue is not feasible without using the IOD results to inform observations with other instruments.

Finally, we also report followup observations of the debris cloud ~5 months after the fragmentation. The observations, as illustrated in Figs. 21 and 22, show a visible debris cloud that is still fairly compact. These observations could be used to infer fragmentation parameters and long-term evolution of the debris cloud, a topic left for future work.

With the increasing amount of infrastructure in space, such as the launches of satellite mega-constellations, the frequency of fragmentation events is unfortunately likely to increase as well. As such, any instrumentation that can assist in mitigating the initial risk posed by the new fragments is a highly valuable asset in space safety.

CRediT authorship contribution statement

Daniel Kastinen: Conceptualization and writing of this study, Methodology, Software, Observations. **Juha Vierinen:** Software, Observations. **Tom Grydeland:** Software, Writing, Copyediting. **Johan Kero:** Observations, Writing, Copyediting.

Declaration of competing interest

The authors declare that they have no known competing financial interests or personal relationships that could have appeared to influence the work reported in this paper.

Data and code availability

All the implemented software to execute the Methodology described is openly available at public GitHub repositories[9][10]. The raw data is available for download at the EISCAT portal[11] after an embargo period of one year has expired.

Acknowledgments

We gratefully acknowledge the EISCAT staff for their assistance during the experiments and in preparation of data for further analysis. EISCAT is an international association supported by research organizations in China (CRIPR), Finland (SA), Japan (NIPR and ISEE), Norway (NFR), Sweden (VR), and the United Kingdom (UKRI). This work was supported in part by the European Space Agency (ESA) Space Debris Office, under cooperative agreement ESA Contract No.4000132725/20/D/MRP. The authors would also like to thank the three anonymous reviewers for their valuable comments and suggestions that greatly improved final version of the manuscript.

References

[1] N. Johnson, P. Krisko, J.-C. Liou, P. Anz-Meador, NASA's new breakup model of evolve 4.0, Adv. Space Res. 28 (9) (2001) 1377–1384, http://dx.doi.org/10.1016/S0273-1177(01)00423-9, URL https://linkinghub.elsevier.com/retrieve/pii/S0273117701004239.

[2] V. Braun, S. Lemmens, B. Reihs, H. Krag, A. Horstmann, Analysis Of Breakup Events, in: Proc. 7th European Conference on Space Debris, ESA Space Debris Office, Darmstadt, Germany, 2017, p. 13.

[3] ESA, Space debris by the numbers, 2022, URL https://www.esa.int/Safety_Security/Space_Debris/Space_debris_by_the_numbers (Accessed 22 Feb 2022).

[4] ESA, ESA'S Annual Space Environment Report, Technical Report, ESA Space Debris Office, 2021.

[5] D.J. Kessler, B.G. Cour-Palais, Collision frequency of artificial satellites: The creation of a debris belt, J. Geophys. Res. Space Phys. 83 (A6) (1978) 2637–2646, Publisher: Wiley Online Library.

[6] J.C. Liou, A.K. Anilkumar, B. Bastida Virgili, T. Hanada, H. Krag, H. Lewis, M.X.J. Raj, M.M. Rao, A. Rossi, R.K. Sharma, Stability of the future LEO environment- an IADC comparison study, in: L. Ouwehand (Ed.), 6th European Conference on Space Debris, in: ESA special publication, vol.723, 2013, p. 2, URL https://ui.adsabs.harvard.edu/abs/2013ESASP.723E...2L.

[7] A. Rossi, L. Anselmo, A. Cordelli, P. Farinella, C. Pardini, Modelling the evolution of the space debris population, Planet. Space Sci. 46 (11–12) (1998) 1583–1596, Publisher: Elsevier.

[8] A. Rossi, L. Anselmo, C. Pardini, R. Jehn, G.B. Valsecchi, The New Space Debris Mitigation (SDM 4.0) Long Term Evolution Code, in: Proc. 5th European Conference on Space Debris, ESA Space Debris Office, Darmstadt, Germany, 2009, p. 8.

[9] T. Lips, B. Fritsche, A comparison of commonly used re-entry analysis tools, Acta Astronaut. 57 (2–8) (2005) 312–323, http://dx.doi.org/10.1016/j.actaastro.2005.03.010, URL https://linkinghub.elsevier.com/retrieve/pii/S0094576505000767.

[10] W. Ailor, W. Hallman, G. Steckel, M. Weaver, Analysis Of Reentered Debris And Implications For Survivability Modeling, in: Proceedings of the Fourth European Conference on Space Debris, ESA Space Debris Office, Darmstadt, Germany, 2005, p. 6.

[11] L. Schulz, K.-H. Glassmeier, On the anthropogenic and natural injection of matter into Earth's atmosphere, Adv. Space Res. 67 (3) (2021) 1002–1025, http://dx.doi.org/10.1016/j.asr.2020.10.036, URL https://linkinghub.elsevier.com/retrieve/pii/S0273117720307663.

[12] A.C. Boley, M. Byers, Satellite mega-constellations create risks in Low Earth Orbit, the atmosphere and on Earth, Sci. Rep. 11 (1) (2021) 10642, http://dx.doi.org/10.1038/s41598-021-89909-7, URL http://www.nature.com/articles/s41598-021-89909-7.

[13] H. Klinkrad, Space Debris: Models and Risk Analysis, Springer Science & Business Media, 2006.

[9] https://github.com/danielk333/SORTS, commit 4425caac415c6e516a1226e9c8053d33e699b623

[10] https://github.com/jvierine/antisat_analysis, commit 0f9454fd0e71e3021ef67b04110d5ef9c519b244

[11] https://portal.eiscat.se/schedule/

[14] G. Muntoni, G. Montisci, T. Pisanu, P. Andronico, G. Valente, Crowded Space: A Review on Radar Measurements for Space Debris Monitoring and Tracking, Appl. Sci. 11 (4) (2021) 1364, http://dx.doi.org/10.3390/app11041364, URL https://www.mdpi.com/2076-3417/11/4/1364.
[15] R. Jehn, H. Klinkrad, From Measurement Results To Space Debris Environment Models, in: IAA-97, Paris, France: The International Astronautical Federation, Torino, Italy, 1997, p. 9.
[16] S. Flegel, P. Krisko, Modeling the Space Debris Environment with MASTER-2009 and ORDEM2010, in: 38th COSPAR Scientific Assembly, Bremen, Germany, 2010, p. 14, URL https://www.researchgate.net/publication/239751139_Modeling_the_space_debris_environment_with_MASTER2009_and_ORDEM2010.
[17] J. Markkanen, M. Lehtinen, M. Landgraf, Real-time space debris monitoring with EISCAT, Adv. Space Res. 35 (7) (2005) 1197–1209, http://dx.doi.org/10.1016/j.asr.2005.03.038.
[18] J. Vierinen, J. Markkanen, H. Krag, High power large aperture radar observations of the Iridium-COSMOS collision, in: Proc. 5th European Conference on Space Debris, ESA Space Debris Office, Darmstadt, Germany, 2009, p. 10.
[19] J. Vierinen, D. Kastinen, J. Markkanen, T. Grydeland, J. Kero, A. Horstmann, S. Hesselbach, C. Kebschull, E. Røynestad, H. Krag, 2018 Beam-park observations of space debris with the EISCAT radars, in: Proc. 1st NEO and Debris Detection Conference, in: 1, vol.1, ESA Space Safety Programme Office, Darmstadt, Germany, 2019, p. 10, URL https://conference.sdo.esoc.esa.int/proceedings/neosst1/paper/480.
[20] G. Stansbery, Preliminary results from the US participation in the 2000 Beam Park Experiment, in: European Space Agency-Publications-ESA SP, Vol. 473, European Space Agency, 2001, pp. 49–52.
[21] EISCAT Scientific Association, EISCAT UHF antenna acceptance tests, Report, (78/7) EISCAT Scientific Association, 1978.
[22] C.A. Balanis, Antenna Theory: Analysis and Design, John wiley & sons, 2015.
[23] M.E. Paulsen, Radar observations of space debris in polar orbits 2018–2021 (Master thesis), UiT Norges arktiske universitet, 2021, URL https://munin.uit.no/handle/10037/22179.
[24] J. Markkanen, A. Huuskonen, A. Väänänen, Measurements of small-size debris with backscatter of radio waves, Technical Report, ESA/ESOC Technical Management, 2002, p. 108.
[25] W.C. Morchin, Radar Engineer's Sourcebook, Artech House Radar Library, 1993.
[26] J. Hamilton, C.H. Blackwell, R. McSheehy, Q. Juarez, P. Anz-meador, Radar measurements of small debris from HUSIR and HAX, NASA Technical Reports Server, Darmstadt, Germany, 2017.
[27] J. Kero, C. Szasz, T. Nakamura, T. Terasawa, H. Miyamoto, K. Nishimura, A meteor head echo analysis algorithm for the lower VHF band, Ann. Geophys. 30 (4) (2012) 639–659, http://dx.doi.org/10.5194/angeo-30-639-2012, URL https://angeo.copernicus.org/articles/30/639/2012/.
[28] P. Swerling, Probability of detection for fluctuating targets, IEEE Trans. Inform. Theory 6 (2) (1960) 269–308, http://dx.doi.org/10.1109/TIT.1960.1057561, URL http://ieeexplore.ieee.org/document/1057561/.
[29] D. Shnidman, Determination of required SNR values [radar detection], IEEE Trans. Aerosp. Electron. Syst. 38 (3) (2002) 1059–1064, http://dx.doi.org/10.1109/TAES.2002.1039422, URL http://ieeexplore.ieee.org/document/1039422/.
[30] D. Izzo, Revisiting Lambert's problem, Celestial Mech. Dynam. Astronom. 121 (1) (2015) 1–15, http://dx.doi.org/10.1007/s10569-014-9587-y, URL http://link.springer.com/10.1007/s10569-014-9587-y.
[31] E. Stansbery, D. Kessler, T. Tracy, M. Matney, J. Stanley, Characterization of the orbital debris environment from Haystack radar measurements, Adv. Space Res. 16 (11) (1995) 5–16, http://dx.doi.org/10.1016/0273-1177(95)98748-D, URL https://linkinghub.elsevier.com/retrieve/pii/027311779598748D.
[32] D.J. Kessler, Collision probability at low altitudes resulting from elliptical orbits, Adv. Space Res. 10 (3–4) (1990) 393–396, http://dx.doi.org/10.1016/0273-1177(90)90376-B, URL https://linkinghub.elsevier.com/retrieve/pii/027311779090376B.
[33] D.J. Kessler, P.D. Anz-Meador, Critical number of spacecraft in low Earth orbit: using satellite fragmentation data to evaluate the stability of the orbital debris environment, in: H. Sawaya-Lacoste (Ed.), Space Debris, in: ESA special publication, vol.1, 2001, pp. 265–272, URL https://ui.adsabs.harvard.edu/abs/2001ESASP.473..265K.
[34] E. Hairer, S.P. Norsett, G. Wanner, Solving Ordinary, Differential Equations I: Nonstiff Problems, second Ed., (1) Springer-Verlag, 2000.
[35] S.A. Holmes, W.E. Featherstone, A unified approach to the Clenshaw summation and the recursive computation of very high degree and order normalised associated Legendre functions, J. Geod. 76 (5) (2002) 279–299, http://dx.doi.org/10.1007/s00190-002-0216-2, URL http://link.springer.com/10.1007/s00190-002-0216-2.
[36] S. Bruinsma, G. Thuillier, F. Barlier, The DTM-2000 empirical thermosphere model with new data assimilation and constraints at lower boundary: accuracy and properties, J. Atmos. Sol.-Terr. Phys. 65 (9) (2003) 1053–1070, http://dx.doi.org/10.1016/S1364-6826(03)00137-8, URL https://linkinghub.elsevier.com/retrieve/pii/S1364682603001378.
[37] D.A. Vallado, P. Crawford, R. Hujsak, T. Kelso, Revisiting spacetrack report# 3, AIAA 6753 (2006) (2006) 446.
[38] F. Gao, L. Han, Implementing the Nelder-Mead simplex algorithm with adaptive parameters, Comput. Optim. Appl. 51 (1) (2012) 259–277, Publisher: Springer.
[39] H. Haario, E. Saksman, J. Tamminen, Componentwise adaptation for high dimensional MCMC, Comput. Statist. 20 (2) (2005) 265–273, Publisher: Springer.
[40] R. McElreath, Statistical Rethinking: A Bayesian Course with Examples in R and Stan, Chapman and Hall/CRC, 2018.
[41] J. Vierinen, D. Kastinen, J. Kero, T. Grydeland, D. McKay, E. Røynestad, S. Hesselbach, C. Kebschull, H. Krag, EISCAT 3D Performance Analysis, Technical Report, ESA/ESOC Technical Management, 2019.
[42] U. Brändström, P. Hyvönen, D. Kastinen, J. Kero, T. Sergienko, ALIS_4D NRFP3 Report, Technical Report, (5.4-12/21) Swedish Institute of Space Physics (IRF), 2022.
[43] D. McKay, T. Grydeland, J. Vierinen, D. Kastinen, J. Kero, K.A. Høgda, White paper Conversion of the EISCAT VHF antenna into the Troms Space Debris Radar, Technical Report, Norut / NORCE Norwegian Research Centre AS, 2019.
[44] J.A. Christian, W.E. Parker, Initial Orbit Determination from Bearing and Range-Rate Measurements Using the Orbital Hodograph, J. Guid. Control Dyn. 44 (2) (2021) 370–378, http://dx.doi.org/10.2514/1.G005433, URL https://arc.aiaa.org/doi/10.2514/1.G005433.